

Star Formation Rates, Metallicities, and Stellar Masses on kpc-scales in TNG50

JIA QI,¹ ALEX M. GARCIA,² PAUL TORREY,² JORGE MORENO,^{3,4} KARA N. GREEN,² AARON S. EVANS,^{2,5} Z. S. HEMLER,⁶
LARS HERNQUIST,⁷ AND SARA L. ELLISON⁸

¹*Department of Astronomy, University of Florida, 211 Bryant Space Sciences Center, Gainesville, FL 32611, USA*

²*Department of Astronomy, University of Virginia, 530 McCormick Road, Charlottesville, VA 22904*

³*Department of Physics and Astronomy, Pomona College, Claremont, CA 91711, USA*

⁴*Carnegie Observatories, Pasadena, CA 91101, USA*

⁵*National Radio Astronomy Observatory, 520 Edgemont Road, Charlottesville, VA 22903*

⁶*Department of Astrophysical Sciences, Princeton University, Peyton Hall, Princeton, NJ, 08544, USA*

⁷*Center for Astrophysics, Harvard & Smithsonian, 60 Garden Street, Cambridge, MA 02138, USA*

⁸*Department of Physics & Astronomy, University of Victoria, Finnerty Road, Victoria, British Columbia, V8P 1A1, Canada*

ABSTRACT

Integral field units (IFU) have extended our knowledge of galactic properties to kpc (or, sometimes, even smaller) patches of galaxies. These scales are where the physics driving galaxy evolution (feedback, chemical enrichment, etc.) take place. Quantifying the spatially-resolved properties of galaxies, both observationally and theoretically, is therefore critical to our understanding of galaxy evolution. To this end, we investigate spatially-resolved scaling relations within central galaxies ($M_{\star} > 10^{9.0}$) at $z = 0$ in IllustrisTNG. We examine both the resolved star-forming main sequence (rSFMS) and the resolved mass-metallicity relation (rMZR) using $1 \text{ kpc} \times 1 \text{ kpc}$ maps of galaxies. We find that the rSFMS in IllustrisTNG is well-described by a power-law, but has some dependence on the host galaxy’s mass. Conversely, the rMZR for IllustrisTNG can be described by a single power-law at low stellar mass surface density that flattens at high surface densities and is independent of host galaxy mass. We find quantitative agreement in both the rSFMS and rMZR with recent IFU observational campaigns. Furthermore, we argue that the rSFMS is an indirect result of the Schmidt-Kennicutt (SK) law and local gas fraction relation, which are both independent of host galaxy properties. Finally, we expand upon a localized leaky-box model to study the evolution of idealized spaxels and find that it provides a good description of these resolved relations. The degree of agreement, however, between idealized spaxels and simulated spaxels depends on the ‘net’ outflow rate for the spaxel, and the observed scaling relations indicate a preference for a low net outflow rate.

Keywords: Galaxy structure(622) — Galaxy formation(595)

1. INTRODUCTION

Scaling relations have long held an important role in describing the nature of galaxies. Perhaps unsurprisingly, galaxies do not have randomly assigned properties, but instead follow well-defined relations. These scaling relations typically compare one integrated property of a galaxy against another (e.g., velocity dispersion and absolute magnitude; Faber & Jackson 1976). However, with the advent of integral field spectroscopy (IFS) surveys (e.g., CALIFA; Sánchez et al. 2012, SAMI; Bryant et al. 2015, MaNGA; Bundy et al. 2015, PHANGS; Leroy et al. 2021), these “global” scaling relations have been extended down to spatially-resolved scales of $\lesssim 1 \text{ kpc}$ (see Sánchez 2020, for a recent review). Indeed,

many of the physical processes that shape global galaxy properties, such as star formation, stellar feedback, and metal redistribution are local processes. Moreover, up to this point, most large-box galaxy evolutionary simulation models are assessed solely on their ability to reproduce global galaxy properties (Vogelsberger et al. 2013; Torrey et al. 2014; Schaye et al. 2015; Donnari et al. 2019). Yet, the important physics underpinning these models occurs on sub-galactic scales. Spatially resolved galaxy scaling relations can provide diagnostics for galaxies’ star formation (Wuyts et al. 2013; Hemmati et al. 2014; Ellison et al. 2020; Hani et al. 2020; Pessa et al. 2021; Baker et al. 2022), metallicity evolution (Rosales-Ortega et al. 2012; Sánchez et al. 2013,

2019; Patrício et al. 2019; Hemler et al. 2021; Garcia et al. 2023), and formation history (Liu et al. 2018; Moreno et al. 2021; Nelson et al. 2021). It is therefore critically important to understand galaxies on not just global scales, but local as well. Quantifying the resolved scaling relations, both in observations and simulation models, is a frontier in our understanding of galaxy evolution.

One scaling relation of interest is the star formation main sequence (SFMS): a tight power-law relation between galactic star formation rate (SFR) and stellar mass (M_*) in normal star forming disk galaxies such that galaxies with larger stellar masses tend to have higher SFRs. The global SFMS relation has been observed in surveys at various redshifts (Brinchmann et al. 2004; Noeske et al. 2007; Daddi et al. 2007; Elbaz et al. 2007; Leslie et al. 2020; Popesso et al. 2023; Koprowski et al. 2024) as well as reasonably well-reproduced by large-scale cosmological simulations (Davé et al. 2011; Torrey et al. 2014; Furlong et al. 2015; Sparre et al. 2015). The overall normalization and power-law index of the SFMS are widely debated in the literature. Generally speaking, though, the power-law index falls between 0.7-1.3 (e.g., Noeske et al. 2007; Lee et al. 2015; Tomczak et al. 2016), but the normalization can vary significantly depending on chosen SFR indicator, sample selection, and/or assumed initial mass function (Speagle et al. 2014).

IFS surveys have now measured a *resolved* star formation main sequence (rSFMS) on kpc-scales of galaxies (e.g., Wuyts et al. 2013; Hemmati et al. 2014; Maragkoudakis 2017; Ellison et al. 2018, 2020; Abdurro'uf & Akiyama 2019). The rSFMS is a power-law relation between the star-formation rate surface density (Σ_{SFR}) and stellar mass surface density (Σ_*). The power-law index of the rSFMS is qualitatively similar to that of the global SFMS, with surveys reporting values ranging from 0.7-1.1 (Cano-Díaz et al. 2016; Hsieh et al. 2017; Medling et al. 2018; Morselli et al. 2020; Ellison et al. 2021; Pessa et al. 2021). Interestingly, the rSFMS appears to be relatively invariant with respect to host mass (Erroz-Ferrer et al. 2019; Enia et al. 2020, although the detailed morphology can change this picture; see, e.g., Maragkoudakis 2017; Medling et al. 2018). Other factors such as active galactic nuclei (AGN) activity (Cano-Díaz et al. 2016 2019, Sánchez et al. 2018), galaxy-galaxy interactions (Pan et al. 2019; Thorp et al. 2019, 2022; Brown et al. 2023a), and/or environment (Medling et al. 2018; Vulcani et al. 2020; Sánchez-García et al. 2022; Brown et al. 2023b, Green et al. In Preparation) can play a significant role in shaping the star formation activity for individual systems.

Another scaling relation used as a benchmark for galaxy evolutionary models is the relationship between a galaxy's stellar mass and gas-phase metallicity (henceforth mass-metallicity relation, or MZR; see, e.g., Tremonti et al. 2004, Lee et al. 2006, Kewley & Ellison 2008 for observational perspective and, e.g., Davé et al. 2011, Torrey et al. 2017, Garcia et al. 2024a 2024b for theory perspective). Similar to the SFMS, the MZR provides insight into the star formation history; however, unlike the SFMS, the MZR essentially contains a “fossil record” of all previous enrichment and gas mixing within the galaxy. Heavy metals are formed in within stars and then ejected into the interstellar medium (ISM) via supernova explosions and asymptotic giant branch winds. Once in the ISM, these metals mix via galactic winds and turbulence (Lacey & Fall 1985; Koeppen 1994; Elmegreen 1999) and are diluted by pristine gas inflows from the circum- and inter-galactic media (Somerville & Davé 2015). The overall metal content, or metallicity, of a galaxy is therefore an imprint of the processes driving the formation and evolution of galaxies.

The MZR also shares some qualitative similarities to the SFMS. The MZR is also a positive power-law correlation for low mass galaxies ($M_* < 10^{10.0} M_\odot$) which flattens, or even turns over, for high mass galaxies ($M_* > 10^{10.0} M_\odot$; see, e.g., Berg et al. 2012, Andrews & Martini 2013, Blanc et al. 2019, Revalski et al. 2024).

Analogous to the rSFMS, recent IFS surveys have measured a *resolved* MZR (rMZR; e.g., Rosales-Ortega et al. 2012; Sánchez et al. 2013, 2019; Barrera-Ballesteros et al. 2016; Barrera-Ballesteros et al. 2018; Zhu et al. 2017; Gao et al. 2018). Generally, the rMZR follows the same qualitative shape as the MZR: a power-law at low stellar mass surface densities that flattens at the highest stellar mass surface densities. There is some evidence that the rMZR depends on the stellar mass of the host galaxy (Gao et al. 2018; Hwang et al. 2019) although not all surveys agree (Barrera-Ballesteros et al. 2016). Regardless, the same physical arguments are generally true for chemical enrichment on local scales as global scales – the metallicity depends on the competition of new enrichment from stars, gas redistribution (i.e., inflows/outflows), and pristine gas accretion (Zhu et al. 2017).

It is generally agreed upon that the resolved scaling relations have the potential to constrain the physics of feedback-regulated star formation on sub-galactic scales given their dependencies on the small-scale physics of the interstellar medium (ISM; see, e.g., Gurbich et al. 2020, Li et al. 2020, Nobels et al. 2024). In this paper, we extend previous simulations results of star-formation

and metals on kpc-scales (see Trayford & Schaye 2019; Orr & Hopkins 2019; Hani et al. 2020; Motwani et al. 2022; McDonough et al. 2023) to the IllustrisTNG cosmological simulation. We also investigate the dependence (or lack thereof) of the relations on the integrated properties of the host galaxies. We quantify the tightness of the two scaling relations and decouple the scatter of the relation into intrinsic and systematic sources. Finally, we make a theoretical argument for the emergence of the rSFMS based on the leaky-box model (Zhu et al. 2017).

This manuscript is organised as follows. In §2, we review the details of our simulation, methods for generating resolved maps for galaxies, and selection criteria for galaxies and spatially resolved regions. In §3, we present our main results for the two scaling relations, their comparison to observations and peer cosmological simulations, the dependence of the relations on host galaxy properties, and the scatters on the relations as intrinsic and systematic sources. In §3.1, we give a discussion about the rSFMS, as a result of the Kennicutt-Schmidt relation and the equation-of-state applied in IllustrisTNG models. In §4, we present an extension of the leaky-box model to account for the rSFMS and $f_{\text{gas}} - \Sigma_{\star}$ relations. In §5, we summarize and conclude our results, as well as portray the future direction for our project.

2. METHODS

2.1. *IllustrisTNG*

In this paper, we employ data products from The Next Generation (TNG) of Illustris simulations (Pillepich et al. 2018a; Springel et al. 2018; Marinacci et al. 2018; Naiman et al. 2018; Nelson et al. 2018, 2019a). TNG is a series of hydrodynamic cosmological simulations of galaxy formation within the Λ CDM paradigm. The TNG model includes a comprehensive set of physical processes governing galaxy formation: gravity, hydrodynamics, star formation, stellar evolution, chemical enrichment, primordial and metal-line cooling of the gas, stellar feedback with galactic outflows, and black hole formation, growth and feedback (see Pillepich et al. 2018b, for a complete description of the TNG model).

The TNG simulations include three box sizes, each simulated at three resolution levels (Pillepich et al. 2018a). The analysis in this work centers on the highest resolution run of the $(35h^{-1} \text{ Mpc})^3$ box: TNG50-1 (hereafter simply TNG; Nelson et al. 2019b, Pillepich et al. 2019). This simulation contains a total of 2×2160^3 particles and a baryon mass resolution of $8.5 \times 10^4 M_{\odot}$.

Critical for the purposes of this work, the TNG model treats the (unresolved) star-forming ISM with

the Springel & Hernquist (2003) effective equation of state (Vogelsberger et al. 2013). The effective equation of state allows new star particles to form stochastically in dense ($n_{\text{H}} > 0.13 \text{ cm}^{-3}$) ISM. The masses of these star particles are consistent with a Chabrier (2003) initial mass function. At the end of the lives of stars (the time-scales of which are set by Portinari et al. 1998 and depend on the mass and metallicity of the star), both mass and metals are returned into the ISM through either asymptotic giant branch (AGB) winds or Type II supernovae. The elemental yields of these events follow prescriptions from Nomoto et al. (1997), Portinari et al. (1998), Kobayashi et al. (2006), Karakas (2010), Doherty et al. (2014), and Fishlock et al. (2014). TNG explicitly tracks 9 chemical species (H, He, C, N, O, Ne, Mg, Si, and Fe) as well as a tenth “other metals” field which is a proxy for the metal species not explicitly tracked.

The TNG model also includes contributions from active galactic nuclei (AGN) in addition to stellar evolution and feedback (see Weinberger et al. 2017, for a complete review of the TNG AGN model). Briefly, TNG implements black hole-driven feedback in two modes: low and high accretion. The high-accretion rate mode of AGN feedback (also referred to as “quasar mode”) provides thermal energy into the surrounding gas; whereas, the low-accretion rate mode (“radio mode”) implements kinetic feedback in the form of black hole driven winds. The net result of the AGN feedback within the TNG simulations is to significantly reduce the star formation in the most massive halos (Weinberger et al. 2017).

2.2. *Galaxy Identification and Sample Selection*

Dark matter haloes are identified using a friends-of-friends (FOF) algorithm (Davis et al. 1985) in TNG, from which individual galaxies are identified using the SUBFIND algorithm (Springel et al. 2001). From these SUBFIND-identified galaxies, we impose three general selection criteria. First, we require all simulated galaxies to have stellar masses $M_{\star} > 10^9 M_{\odot}$. This mass selection criterion ensures that our selected galaxies have a large enough number of particles (i.e. $> 10^4$) to construct property maps with resolved spatial variations. Secondly, we use a specific star formation rate (sSFR) threshold of $\text{sSFR} > 10^{-10} \text{ yr}^{-1}$ to select star-forming galaxies (i.e., those that are not significantly below the global star formation main sequence at $z = 0$). The second selection criterion also ensures that there are star-forming gas cells *somewhere* within the system. This is desirable as observational metallicity measurements are strictly limited emission from bright star forming regions in galaxies (Kewley & Ellison 2008; Kewley et al.

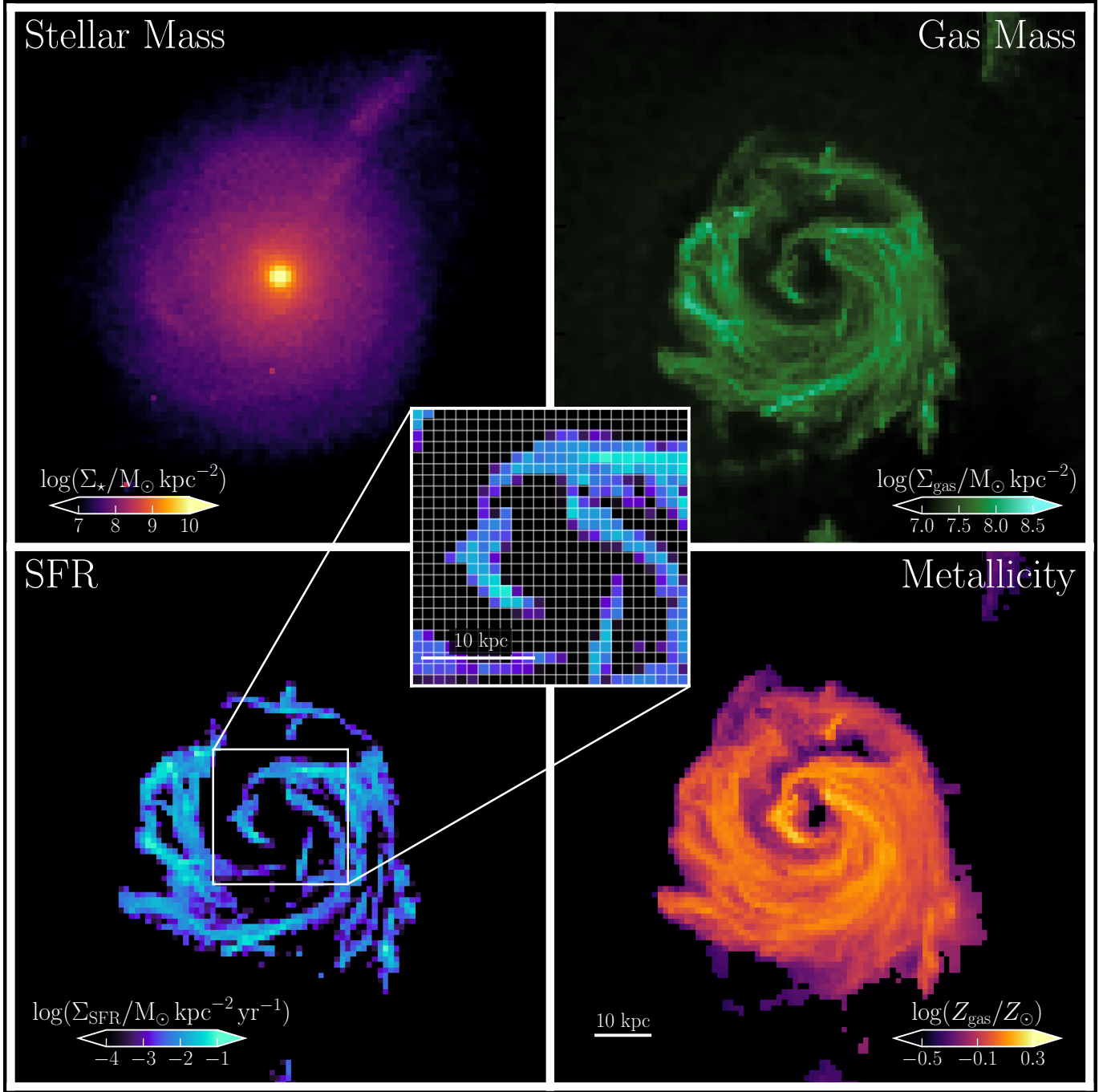


Figure 1. Example of Our Spaxel Construction in IllustrisTNG. Representative face-on maps from the TNG50-1 simulation of a galaxy at 1-kpc spaxel resolution. We present maps of the stellar mass surface density (Σ_* ; upper left), gas mass surface density (Σ_{gas} ; upper right), star formation rate surface density (Σ_{SFR} ; lower left), and mass-weighted gas-phase metallicity (lower right). The field-of-view for the large maps are 100 kpc and each spaxel has a size of 1 kpc \times 1 kpc. The central panel shows a zoom-in of the central region of the galaxy in SFR surface density projection. We note that these images are down-sampled from the native TNG resolution to be closer to the resolution of current IFS surveys.

2019; Maiolino & Mannucci 2019). Finally, to minimize the impact from the halo substructure, we use only the central galaxy of each identified FOF group. This means that material from satellite galaxies will not be accounted for in the reconstructed spaxel maps. Taken together, these selection criteria yield 2,640 galaxies at $z = 0$.

2.3. Resolved spaxel maps

A central goal of this work is to compare the TNG simulated resolved galaxy scaling relations against observations – specifically those of CALIFA (Sánchez et al. 2012), MaNGA (Bundy et al. 2015) and PHANGS (Leroy et al. 2021). Such campaigns investigate the rSFMS and gas-phase rMZR with the resolution of about 1 kpc at low redshift ($z < 0.1$; Maragkoudakis 2017). We note that (at $z = 0$) the smallest hydrodynamical gas cells in TNG have an extent of 48 pc and most baryonic cells are smaller than 1 kpc – slightly higher than these current IFS studies. Our spaxel map construction choices, therefore, do not represent the native spatial resolution of TNG; instead, they are adjusted to be more comparable to the resolution of observations.

We create two-dimensional maps of our galaxies for each relevant galaxy property for this study: the stellar mass surface density (Σ_*), gas mass surface density (Σ_{gas}), star formation rate surface density (Σ_{SFR}), and gas phase metallicity (each illustrated in Figure 1). This set of maps allows us to construct additional relevant quantities such as gas fractions, gas depletion timescales, and star formation efficiencies. The pixel (spaxel) size in these images (and, indeed, in the entirety of our analysis) is set to a fixed value of 1 kpc on the side. To construct these spaxel maps, we extract particles associated with an individual galaxy based on the FOF halo assignments. We then center the galaxy based on its center-of-mass. Next, we rotate the galaxy to a face-on orientation by calculating the net angular momentum vector for all gas particles within 5 kpc of the galactic center and aligning that angular momentum vector to the \hat{z} direction. This alignment maximizes the number of valid spaxels within each galaxy and promotes a fair comparison with the observed datasets, which preferentially select low-inclination systems¹. We note that our method for disk alignment is imperfect for a subset of

systems, especially those with warped disks; however, this method efficiently brings the majority of systems into face-on alignment. Moreover, the small residual angular offsets away from perfect face-on orientation in these warped systems would not significantly affect our main results. Finally, we create a 3D grid for each property of interest (i.e., stellar mass, gas mass, SFR, and gas-mass-weighted gas metallicity) by mapping the discrete particle distributions onto a 3D grid using a traditional smoothing method with a cubic spline kernel. This 3D grid is then converted into a 2D map by integrating over the \hat{z} direction for each 2D spaxel. We do not expect modifying this procedure – e.g., by including a modified smoothing kernel – to alter our results (Trayford & Schaye 2019).

We require that individual spaxels to contain stellar mass surface densities of $\Sigma_* > 10^7 M_\odot \text{kpc}^{-2}$, and star formation rate surface densities of $\Sigma_{\text{SFR}} > 10^{-4} M_\odot \text{yr}^{-1} \text{kpc}^{-2}$ (the later of which implicitly requires the presence of gas mass). From the 2,640 selected galaxies, we end up with 347,006 star-forming spaxels that are used in our analysis.

3. RESULTS

3.1. The Resolved Star Formation Main Sequence (rSFMS)

We present the $z = 0$ rSFMS from TNG in Figure 2. The 2D histogram shows the distribution of all valid spaxels from the TNG galaxy population, with darker histogram pixels indicating more spaxels in that bin. The thick solid orange line represents the median of the distribution, with the shaded orange region representing the 16-84th percentile of the distribution. Typically the rSFMS is fit with a power-law described by

$$\Sigma_* = \beta \Sigma_{\text{SFR}}^\alpha, \quad (1)$$

where α is the power-law index (i.e., slope in log-log space) and β is the scaling coefficient. Indeed, the median relation in TNG is well-described by this power-law relation with an index of $\alpha = 0.606$ in the range $\Sigma_* = 10^7 - 10^9 M_\odot \text{kpc}^{-2}$. We also include the median (or best-fit, in some cases) rSFMS from recent IFS surveys: CALIFA as the dashed orange line (from Cano-Díaz et al. 2016), MaNGA as the dotted red line (from Hsieh et al. 2017), ALMaQUEST in the dot-dashed red line (from Ellison et al. 2021), and PHANGS as the solid purple line (from Pessa et al. 2021). The power-law indices from these observational surveys align reasonably well with that of TNG (see also Medling et al. 2018;

¹ Recently, EDGE-CALIFA (Bolatto et al. 2017) and GECKOS (van de Sande et al. 2024) have begun to include edge-on or highly inclined systems. While interesting comparisons exist between these edge-on surveys, we opt to primarily focus on face-on systems and ignore inclination effects in this work.

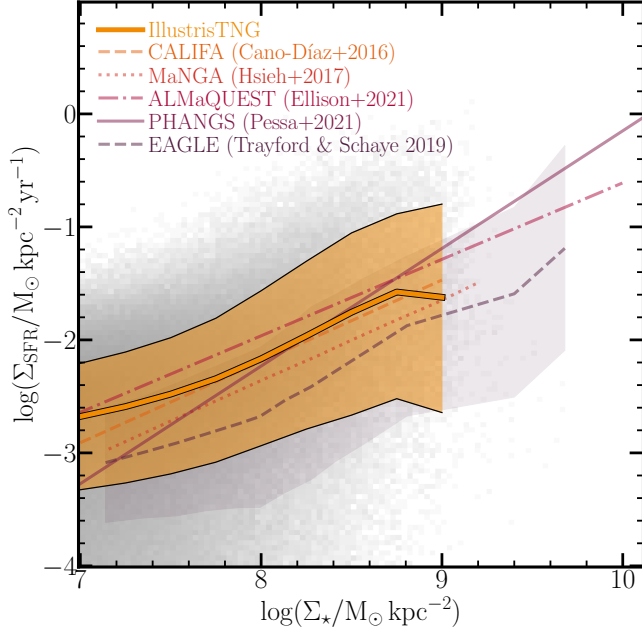


Figure 2. The Resolved Star Formation Main Sequence (rSFMS) in IllustrisTNG The rSFMS in TNG at $z = 0$ with 1 kpc spaxel resolution. The solid orange line shows the median value of Σ_{SFR} in each Σ_* bin, whilst the two dashed orange lines indicate the 16th-84th percentiles. The background 2D distribution displays our selected spaxels, color-coded by the number in each bin. For comparison, we show the rSFMS from the EAGLE simulation (Trayford & Schaye 2019) in the dashed line (and shaded region about it), observational results from the MaNGA survey (Hsieh et al. 2017) in the dotted line, from the CALIFA survey (Cano-Díaz et al. 2016) in the red dashed line, and PHANGS survey in the solid black line (Pessa et al. 2021), and ALMaQUEST (Ellison et al. 2021) in the dot-dashed line. We note that for the rSFMS, as well as all other median/percentile binning in this work, we space Σ_* bins in width of 0.25 dex and require 200 spaxels in each bin.

Morselli et al. 2020)². Similarly, the normalization of the rSFMS is reasonably well reproduced by TNG compared to observational surveys. The broad agreement in both slope and normalization of the rSFMS is notable as the TNG physical model is not tuned in any direct way to give rise to the observed rSFMS. Rather, this simulated rSFMS is a consequence of the underlying galaxy formation model already included in TNG (Springel & Hernquist 2003). We also include predictions from the EAGLE simulation (dashed black line; Trayford & Schaye 2019). We find similar agreement between the two different simulation models in terms

² We do note, however, that different fitting procedures can change the slope significantly (see, e.g., Lin et al. 2019; Morselli et al. 2020; Ellison et al. 2021).

of shape and scatter; however, the normalization of the rSFMS in EAGLE is ~ 0.2 dex lower than in TNG. Trayford & Schaye (2019) attribute lower normalization in EAGLE to the global SFMS being -0.2 dex offset in EAGLE (seen in Furlong et al. 2015).

While the global SFMS is a fairly tight relation in TNG, with 1σ scatter of ~ 0.2 dex (e.g., Sparre et al. 2015), the scatter about the rSFMS is more than twice as much, with 1σ scatter of ~ 0.5 dex. The full population of data points about the rSFMS occupy nearly ± 2 dex above and below the median main sequence. We investigate both individual system’s rSFMS and the dependence on host mass within the TNG model in the following sub-sections.

3.1.1. Individual Galaxies

First, we quantify the effect of individual systems by extracting spaxel data for systems with more than 20 valid spaxels (see Section. 2.2 for definition of “valid”) and fit the rSFMS for each individual galaxy³. For brevity, we summarize the results of this analysis with three parameters describing the rSFMS within individual galaxies: (i) Σ_{SFR} at $\Sigma_* = 10^{8.0} M_\odot \text{kpc}^{-2}$, (ii) the best-fitting power-law indexes (α from Equation 1) for individual galaxies, and (iii) the standard deviation of spaxel’s Σ_{SFR} around the regression. Figure 3 shows the distribution of the parameters of individual rSFMS for all galaxies (black line) as well as galaxies within different stellar mass bins (colored lines). The Σ_{SFR} of most systems ranges between $10^{-3.0}$ to $10^{-2.0} M_\odot \text{kpc}^{-2} \text{yr}^{-1}$ at $\Sigma_* = 10^{8.0} M_\odot \text{kpc}^{-2}$, with a median of $10^{-2.45} M_\odot \text{kpc}^{-2} \text{yr}^{-1}$. This median normalization is broadly consistent with the median relation in Figure 2, albeit slightly more negative than the combined population. Lower mass galaxies tend to have higher Σ_{SFR} whereas higher mass galaxies tend to have lower Σ_{SFR} at $\Sigma_* = 10^{8.0} M_\odot \text{kpc}^{-2}$. The offset in median normalization is quite large from lowest to highest mass bins at ~ 1 dex. In contrast, the standard deviation scatter in the right panel of Figure 3 shows the intrinsic pixel-to-pixel variations within the same galaxies. For all galaxies, the 1σ scatter is centered at ~ 0.25 dex, which is markedly less than that of the population’s rSFMS. For individual mass bins, the scatter

³ The choice of 20 valid spaxels is to balance between the meaningful nature of an individual galaxy fit (i.e. fits with very few pixels may easily become noise-dominated) and the total number of galaxies analyzed. With too few valid spaxels, we cannot fit a meaningful rSFMS for individual spaxels, but requiring too many valid spaxels significantly reduces the number of available galaxies. We note that our key results are not sensitive to this choice of spaxel counts.

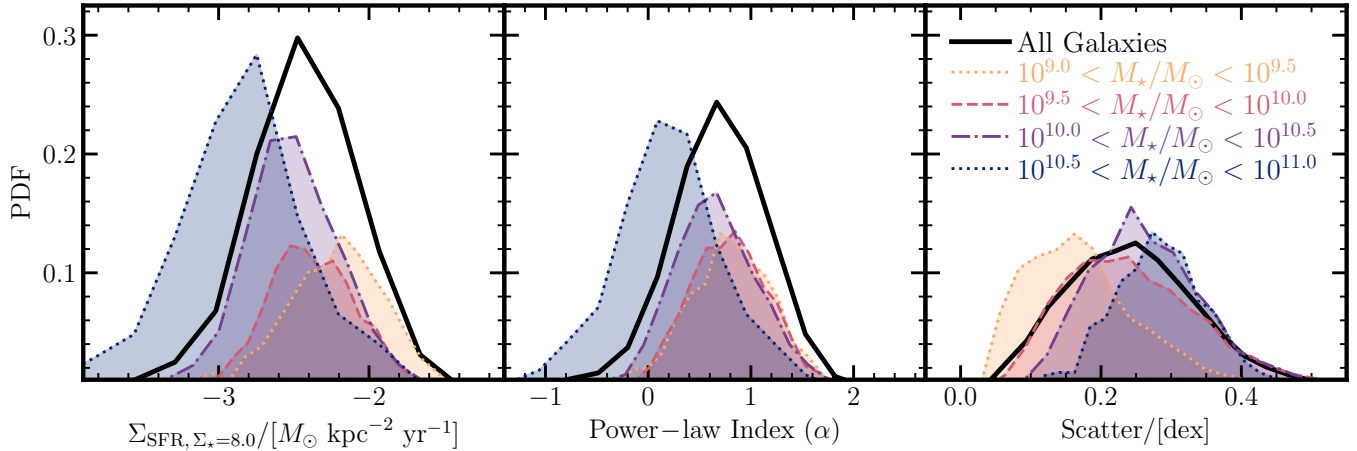


Figure 3. Best-fitting parameters for the rSFMS of individual galaxies. *Left:* The probability distribution function (PDF) of normalizations of the rSFMS for individual galaxies Σ_{SFR} (taken at $\Sigma_* = 10^{8.0} M_\odot$). In all three panels the colored distributions are the individual galaxies’ PDFs broken up by global mass bin and the solid black line is the distribution for all galaxies combined. *Middle:* The PDF of power-law indexes (i.e., α from Equation 1). *Right:* The scatter distribution around their best-fit linear rSFMS model, as measured by the standard deviation of residual.

about rSFMS for individual galaxies is at a similar level, except for the least massive galaxies, which is lower (at ~ 0.15 dex). As expected, the intrinsic scatter of ± 0.25 dex and systematic variation of 0.6 dex approximately add up to the 0.5 dex 1σ scatter of the rSFMS for all galaxies in Figure 2.

The median power-law index for all individual galaxies is 0.69, which is roughly consistent with (although slightly steeper than) the slope of rSFMS by stacking all spaxels together (0.606). Interestingly, the rSFMS is steeper for lower-mass galaxies and shallower for higher-mass galaxies. In fact, a significant fraction of galaxies even show an anti-correlation between Σ_* and Σ_{SFR} in the highest mass bin ($10^{10.5} < M_* < 10^{11.0} M_\odot$). These inversions are, in all likelihood, caused by AGN feedback, which only effects massive galaxies in the TNG model. AGN have been shown to suppress star-formation rates of galaxies within TNG (Weinberger et al. 2017). Regardless, the contributions from these more massive galaxies, which generally have more valid spaxels, is most likely what causes the difference between the full population power-law index and that of the individual galaxies.

3.1.2. Dependence of rSFMS on Host Galaxy Mass

The second consideration for the scatter within the rSFMS is the dependence on host galaxies. To quantify the dependence on the spaxels’ host, Figure 4 shows the rSFMS for spaxels split into different bins by the stellar mass of their host galaxies. The normalization of each of the mass-binned rSFMS is similar to each other (within 0.05 dex) for stellar mass surface densities below $\Sigma_* < 10^{7.5} M_\odot \text{ kpc}^{-2}$. At higher Σ_* , however, lower mass

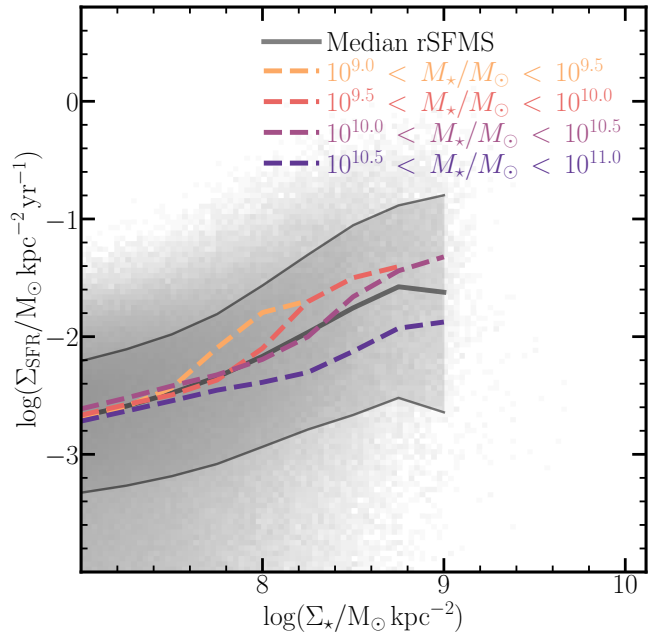


Figure 4. The rSFMS for galaxies binned by total mass. The rSFMS for galaxies within different mass bins as indicated by the title. The black solid line plots the median rSFMS relation and the black dashed line indicates the 1σ scatter. The colored background shows the distribution of spaxels, the same as Figure 2.

systems tend to have higher Σ_{SFR} . This break to higher star formation rate surface density is especially true for the lowest three mass bins. The slope of the rSFMS remains roughly constant until $\Sigma_* \approx 10^{7.5}$ in the lowest total mass bin, $\approx 10^{7.8}$ in the second lowest total mass bin, and $\approx 10^{8.3}$ for the second highest mass bin. At this break the SFR surface density jumps by $\sim 0.3 - 0.4$ dex.

Mass bin ($\log M_{\odot}$)	Power-Law (α)	Coefficient (β)
All	0.606	-6.979
9.0 – 9.5	0.876	-8.903
9.5 – 10.0	0.803	-8.428
10.0 – 10.5	0.683	-7.522
10.5 – 11.0	0.431	-5.781

Table 1. rSFMS fit parameters. The best-fit power-law index (α) and scaling coefficient (β) of Equation 1 for each stellar mass bin’s rSFMS as well as the total rSFMS. We note that the individual mass bins’ rSFMS are not as well conditioned by a single power-law (see footnote 4).

The jump in Σ_{SFR} is subsequently followed by a flattening around 0.4 dex higher in Σ_{\star} . We note, however, that the highest mass bin does not show as significant of a break, although there is a modest jump of ~ 0.2 dex in Σ_{SFR} around $\Sigma_{\star} = 10^{8.3} M_{\odot} \text{ kpc}^{-2}$. To put the differences between the different mass bins more concretely, we fit each mass bin with its own power-law (of the same form as Equation 1)⁴. We present the power-law index and scaling coefficient for the rSFMS mass bins in Table 1. We find that with increasing mass bin the power-law index decreases, while the scaling coefficient increases. We explore the origin of this mass dependence within the rSFMS in Section 4.1.1; however, for now, we note that it comprises some total fraction of the observed scatter in the rSFMS.

3.2. The Resolved Mass Metallicity Relation (rMZR)

Figure 5 shows the rMZR at $z = 0$ from TNG. The background 2D histogram shows the full distribution of spaxels, while the solid line indicates the median rMZR relation and the shaded region is 16th-84th percentile range. The rMZR of TNG follows the same general shape as the integrated MZR: a power-law at low stellar mass (surface densities) with a flattening at the highest masses. More specifically, the median rMZR is well-described by a positive power-law below a surface density $\Sigma_{\star} < 10^{8.5} M_{\odot} \text{ kpc}^{-2}$ with a power-law index of 0.25. Above $\Sigma_{\star} \sim 10^{8.5} M_{\odot} \text{ kpc}^{-2}$, however, the relation flattens significantly and plateaus. These high- Σ_{\star} spaxels tend to inhabit the central regions ($r \lesssim 2 \text{ kpc}$) of massive galaxies (see discussion in Section 4.1). The spaxels at small galactocentric distances are therefore

⁴ We note that the individual mass bin rSFMS are not strictly a power-law relation, particularly in the lower mass bins (see previous discussion). Regardless, quantifying the different bins in this way allows us to include: (i) the different locations of the jump in the Σ_{SFR} as well as (ii) the overall change in normalization at this jump.

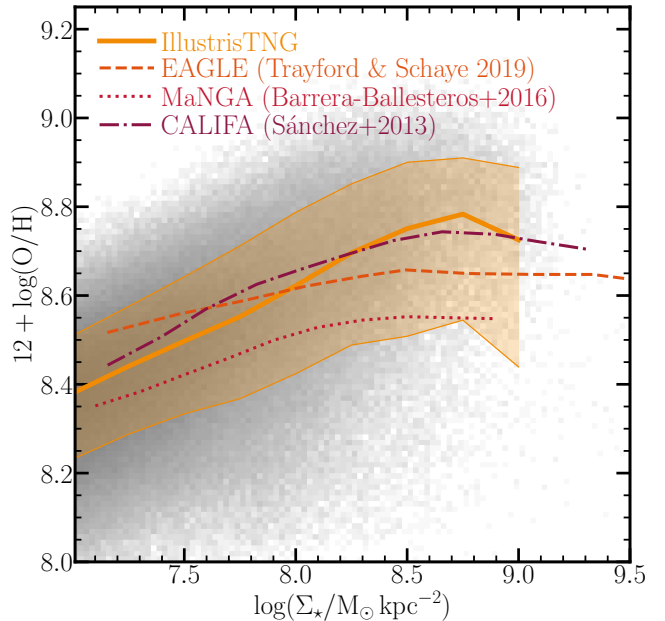


Figure 5. The Resolved Mass Metallicity Relation (rMZR) in IllustrisTNG. The rMZR in TNG at $z = 0$ with spaxel resolution of 1 kpc. The solid line shows the median value of $12 + \log(\text{O}/\text{H})$ and the shaded region indicates the 16th-84th percentile scatter of the background distribution of spaxels. For comparison, the dashed line is the analogous result from the EAGLE simulation (Trayford & Schaye 2019). The dotted line is from the MaNGA survey (Barrera-Ballesteros et al. 2016) and the dash-dotted line is from the CALIFA survey (Sanchez et al. 2013). We caution against too strong a comparison against observational results, however; see text for more details.

likely to be strongly affected by AGN-driven outflows in the TNG model (see Section 2.1 and Weinberger et al. 2017 for more details on TNG AGN modeling).

Next, we compare against observations – CALIFA (Sanchez et al. 2013) and MaNGA (Barrera-Ballesteros et al. 2016) – as well as other simulation results (EAGLE, Trayford & Schaye 2019). We caution against too strong a comparison between the rMZR of TNG with that of observations as the derived metallicities from the IFS surveys are dependent on the chosen diagnostic (Kewley & Ellison 2008; Kewley et al. 2019; Maiolino & Mannucci 2019). Moreover, the normalization of the EAGLE rMZR from Trayford & Schaye (2019) was adjusted to be closer to that of observations (by -0.6 dex). We therefore strongly advocate against a detailed comparison of the normalization of the rMZR without a more careful treatment of the diagnostics. Regardless, we opt to make the comparison of the *qualitative* shape of the rMZR in order to directly compare our results to

previous results⁵. We find that the shape of the rMZR in IllustrisTNG broadly matches its observational counterparts and EAGLE predictions. Their common characteristics are captured in the IllustrisTNG result: as a positive power-law for low Σ_* regime and a flattening/turnover for high Σ_* . The TNG rMZR is steeper than that of MaNGA and EAGLE for the positively-correlated low Σ_* regime, but quite similar to that of CALIFA. Similarly, the flattening starts at a lower Σ_* in EAGLE and MaNGA, but is reasonably similar to CALIFA.

3.2.1. Dependence on Star Formation Rates

In both observations (e.g., Ellison et al. 2008; Lara-López et al. 2010; Mannucci et al. 2010; Belli et al. 2013; Sanders et al. 2018) and simulations (De Rossi et al. 2015; Torrey et al. 2018; Garcia et al. 2024a,b) the scatter about the global MZR is anti-correlated with the star formation rate. This anti-correlation between a galaxy’s SFR and metal content is oftentimes referred to as the Fundamental Metallicity Relation (or FMR). Yet, it is unclear whether this “fundamental” relation holds on sub-galactic scales between Σ_* , Σ_{SFR} , and local metallicity (see Sánchez et al. 2013; Barrera-Ballesteros et al. 2016, 2017; Sánchez-Menguiano et al. 2019; Trayford & Schaye 2019; Ji & Yan 2022; Schaefer et al. 2022; Baker et al. 2023a, Koller et al. 2024).

We present the *resolved* Fundamental Metallicity Relation (rFMR) from TNG in two different ways in Figure 6: (i) the left-panel shows the rMZR with lines color-coded by their star formation rate surface densities, and (ii) the right-hand panel of Figure 6 shows the rMZR color-coded by each pixel’s average offset from the rSMFS. In both representations of the rFMR, we find that, at low Σ_* ($\sim 7.0 - 7.5 \log[M_\odot \text{ kpc}^{-2}]$), there is virtually no dependence on the SFR of the spaxel. At higher Σ_* , however, there appears to be some residual trend: spaxels with higher SFRs tend to have higher metallicities. We note that this is the *opposite* trend as the integrated FMR. This result is potentially in tension with observations from Baker et al. (2023a). Those authors find that the rFMR follows the same trend as the integrated FMR in a MaNGA sample; though it should be noted that the anti-correlation with SFR appears to weaken with increasing Σ_* in that work. Other observational works, however, seem to suggest there is no strong correlation between Σ_{SFR} and Z_{gas} at all (see, e.g., Sánchez et al. 2013; Ji & Yan 2022). It is there-

fore unclear the extent to which the inverted rFMR is in tension with observations.

Interestingly, the inversion of the correlation between Σ_{SFR} and Z_{gas} is also reported in EAGLE (Trayford & Schaye 2019), though it is less ubiquitous across Σ_* . The inversion of the rFMR in EAGLE occurs at $\Sigma_* \sim 10^8 M_\odot \text{ kpc}^{-2}$ and is attributed to the transition from SF feedback dominated to AGN feedback dominated spaxels. In TNG, however, the inversion appears to be a feature of radial dependence on both of metallicity and SFR within galaxies. Inner regions of the galaxies in TNG typically have both: (i) higher metallicity (e.g., Hemler et al. 2021; Garcia et al. 2023) and (ii) higher Σ_{SFR} (Wang et al. 2018; Wang & Lilly 2023) than the outskirts. The inset on the right-hand panel of Figure 6 shows the offsets from the rSFMS (abscissa) and rMZR (ordinate) color-coded by the mean galactocentric distance of each histogram pixel. There are a couple of interesting trends within the offset-offset diagram. Firstly, generally speaking, the spaxels closest to the center of the galaxy preferentially live in the top right corner of this space (i.e., elevated metallicity and elevated SFRs) while the spaxels furthest from the center of galaxies preferentially lie in the bottom-left of this space (i.e., lower metallicity and lower SFRs). Secondly, there is a subset of spaxels at small radii that lie very negatively offset from the rSFMS. These spaxels are preferentially in galaxies with stellar mass $> 10^{10} M_\odot$. It is therefore likely that these spaxels are from regions near AGN, which actively suppress star formation in the inner regions of these massive galaxies.

3.2.2. Dependence of rMZR on Host Galaxies

Figure 7 shows the rMZR, binned by host galaxies’ total stellar mass. The background histogram, gray median line, and gray shaded region are the same as from Figure 5 while the colored lines represent the median rMZR for spaxels with host stellar masses of $10^{9.0} < M_*/M_\odot < 10^{9.5}$ (orange), $10^{9.5} < M_*/M_\odot < 10^{10.0}$ (dark orange), $10^{10.0} < M_*/M_\odot < 10^{10.5}$ (red), and $10^{10.5} < M_*/M_\odot < 10^{11.0}$ (dark red). For low to intermediate mass galaxies ($M_* < 10^{10.5} M_\odot$), the rMZR closely follow the overall relation. We see a slight (less than 0.1 dex) shift in the normalization of rMZR from lower-mass to higher-mass galaxies, which is significantly less than the scatter within the full population of spaxels. Just as in the full rMZR there is a turnover at large Σ_* but the point of turnover seems to increase with increasing global mass. This shift is possibly caused, in part, by low mass galaxy’s spaxels not occupying the higher Σ_* space. It should also be noted that the median rMZR for galaxies with the to-

⁵ We caution, however, that the shape of the (r)MZR can also depend on diagnostics (see, e.g., Kewley & Ellison 2008).

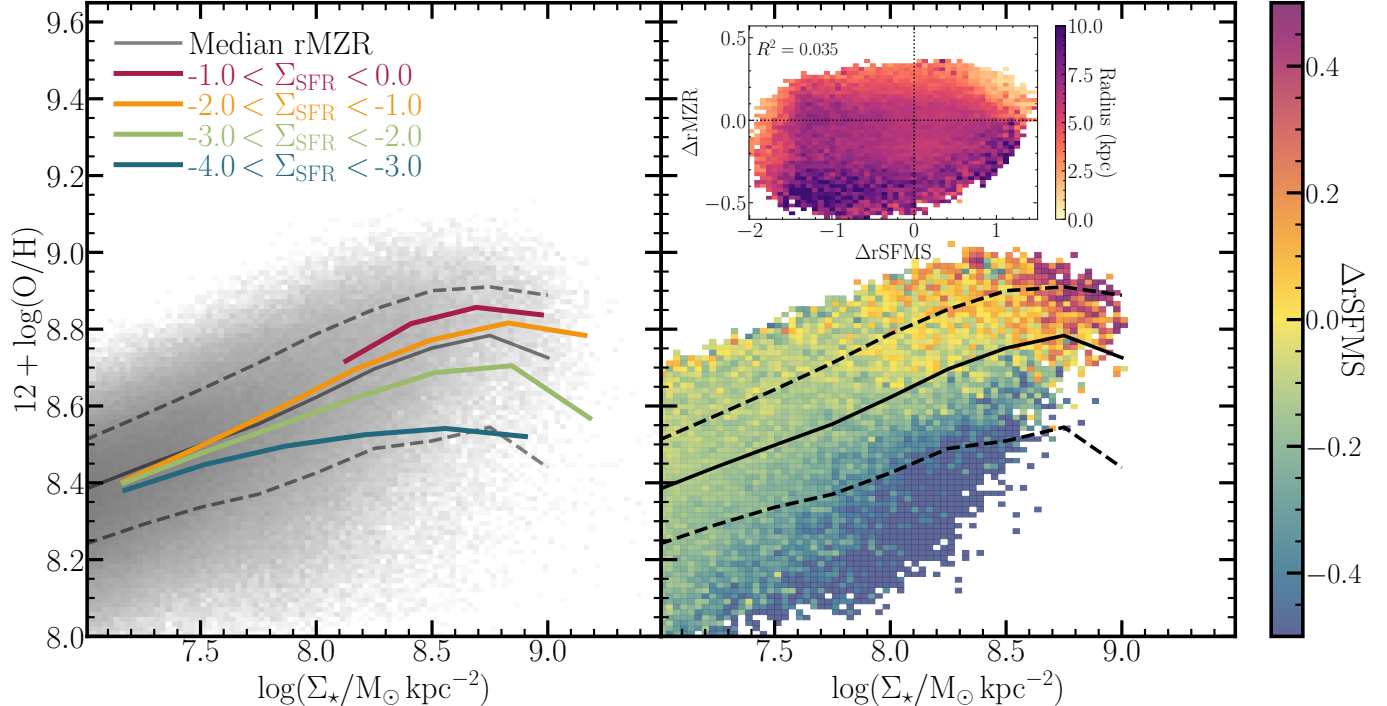


Figure 6. The Resolved Fundamental Metallicity Relation (rFMR) in IllustrisTNG. *Left:* The rMZR for different Σ_{SFR} bins. The 2D histogram in the background is the full distribution of metallicities from TNG (same as Figure 5), while the gray lines are the median (solid) as well as 16th and 84th percentile (dashed) of the distribution. *Right:* The rMZR color-coded by the average spaxel’s offset from the rSFMS. The inset shows the offsets from the rMZR against the offsets from the rSFMS, color coded by the average distance of the spaxels from the galactic center.

tal stellar mass of $10^{10.5-11.0} M_\odot$ shows a much flatter relationship at $\Sigma_* < 10^{8.25} M_\odot \text{ kpc}^{-2}$ than the lower mass counterparts. Furthermore, this highest mass bins’ rMZR seems to not “turn-over” in the same sense as the lower mass bins – instead, it has a sharp increase from $\Sigma_* \approx 10^{8.25} - 10^{8.75} M_\odot \text{ kpc}^{-2}$ which plateaus thereafter. As mentioned previously, strong AGN feedback abruptly becomes effective for galaxies in the TNG model with large stellar masses ($M_* \sim 10^{10} M_\odot$), thus it is perhaps not surprising that the rMZR of these highest mass galaxies should behave differently from other galaxies. Ultimately, despite the differences in the detailed shapes of the mass bins’ median relations, the rMZR shows very little dependence on the host’s total stellar mass in TNG.

4. DISCUSSION

4.1. On the Origin of the rSFMS

To understand the origin of the rSFMS, it is helpful to break down the rSFMS’s dependence on both the star formation efficiency as well as gas content within galaxies. The dependence on star formation efficiency roots in the Schmidt-Kennicutt (SK) relation, which is a well-established relation between Σ_{SFR} and Σ_{gas} with

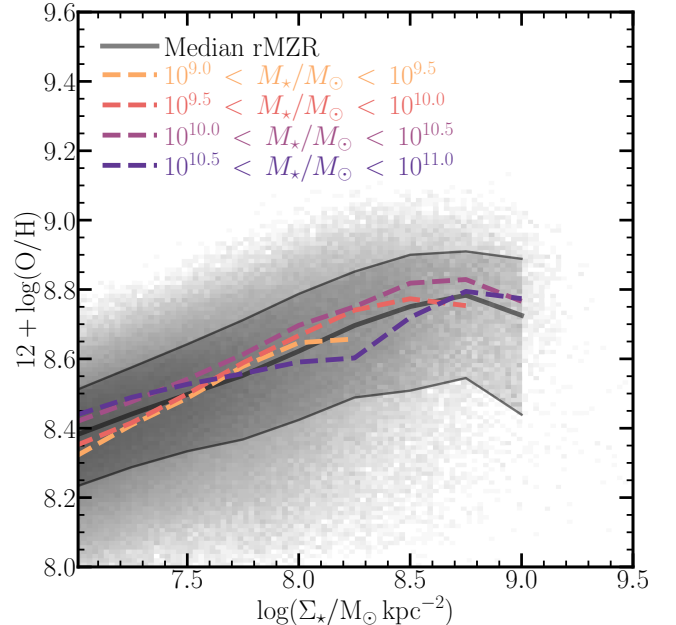


Figure 7. The rMZR for galaxies binned by total mass. The rMZR split into different global stellar-mass bins (colored lines). The black solid line represents the median rMZR and the gray shaded region is the 1σ scatter (same as Figure 5). The background histogram is the full population of spaxels.

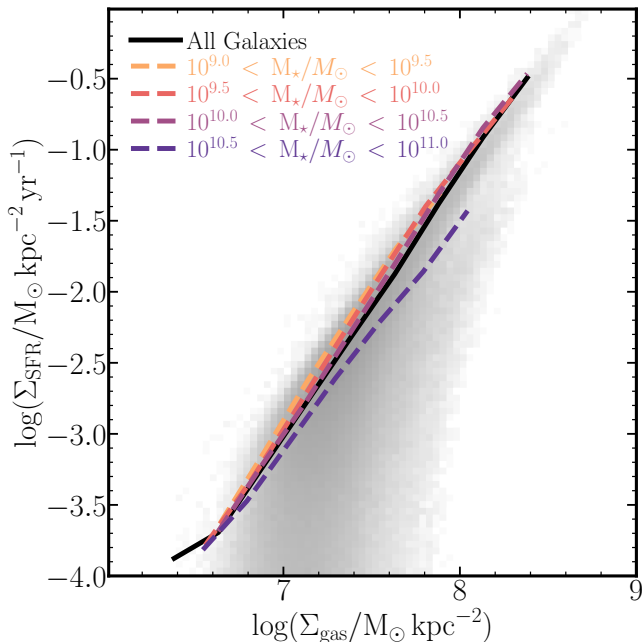


Figure 8. Resolved Schmidt-Kennicutt (SK) relationship in TNG. The SK relation for spaxels in TNG at $z = 0$ with 1 kpc spaxel resolution. The colored lines represent the median SK relation in different mass bins, while the black line represents the median relation including all spaxels. The background histogram is the full population of spaxels.

the form

$$\Sigma_{\text{SFR}} = \epsilon \Sigma_{\text{gas}}^k, \quad (2)$$

where ϵ is star formation efficiency and k is the power-law index (Schmidt 1959; Kennicutt 1998). Figure 8 shows the median SK relation for all TNG spaxels (solid black line) as well as in the different mass bins (dashed colored lines). In both the full population and within mass bins, there is a tight positive correlation between Σ_{SFR} and Σ_{gas} with $\epsilon = 4.78 \times 10^{-16}$ and $k = 1.77$. The tight correlation is expected behavior since the TNG model (along with the Illustris, EAGLE, and similar models with sub-grid ISM prescriptions) manually implements a version of the SK relation via the gas physical (3D) density where $\dot{\rho}_* \propto \rho_{\text{gas}}^a$. This implementation enforces that star-forming gas (i.e. gas with densities above the star formation density threshold; $n_H = 0.13 \text{ cm}^{-3}$, as in Springel & Hernquist 2003) broadly reproduces the SK relation, with $a \sim 1.5$. We therefore stress that the tightness of the “resolved” version of SK relation likely follows from this prescription. Within the individual mass bins, we find that systems with $M_* < 10^{10.5} M_\odot$ are similar to the median relation. Systems with $M_* > 10^{11.0} M_\odot$, however, seem to deviate from this trend at higher Σ_{gas} values. We discuss this further in Section 4.1.1.

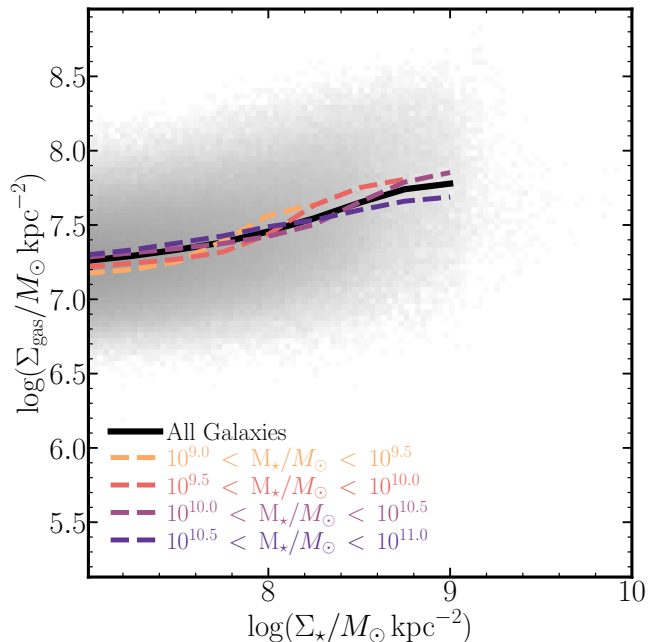


Figure 9. The Gas Mass Main Sequence in IllustrisTNG. The $f_{\text{gas}} - \Sigma_*$ relation in TNG at $z = 0$ with 1 kpc spaxel resolution. The distribution in the background is the full population of spaxels from TNG and the solid black line is the median of this distribution. The dashed colored lines represent the median $f_{\text{gas}} - \Sigma_*$ relation in different stellar mass bins.

Figure 9 shows Σ_{gas} as a function of Σ_* (i.e., the “gas mass main sequence”) for all TNG spaxels (in black) and different mass bins (in colors). We find a power-law trend between Σ_{gas} and Σ_* such that

$$\Sigma_{\text{gas}} \propto \Sigma_*^n, \quad (3)$$

with $n = 0.228$ in TNG. We note that, just as was seen in the rSFMS mass bins, there are “jumps” in the gas content within the different mass bins. The power-law relation breaks downwards at higher values of Σ_* (around $10^9 M_\odot \text{ kpc}^{-2}$). These high- Σ_* spaxels tend to correspond to the central regions of massive galaxies (with $M_* > 10^{10.0} M_\odot$). The break in this relation can therefore be explained by the feedback from their powerful AGNs, which blows away a large portion of their gaseous material but leaves the stellar components relatively unscathed. Regardless, we can combine Equations 2 and 3 to obtain

$$\Sigma_{\text{SFR}} \propto \Sigma_*^{nk}. \quad (4)$$

Equation 4 is of the form of the rSFMS (i.e., Equation 1) with $\alpha = nk$. Combining the measured n and k from earlier in this section, we obtain a value of $\alpha = 0.403$. Admittedly, this approach yields a shallower power-law than measured in Section 3.1 (by around 33%). A source of this discrepancy may come from using a total gas mass

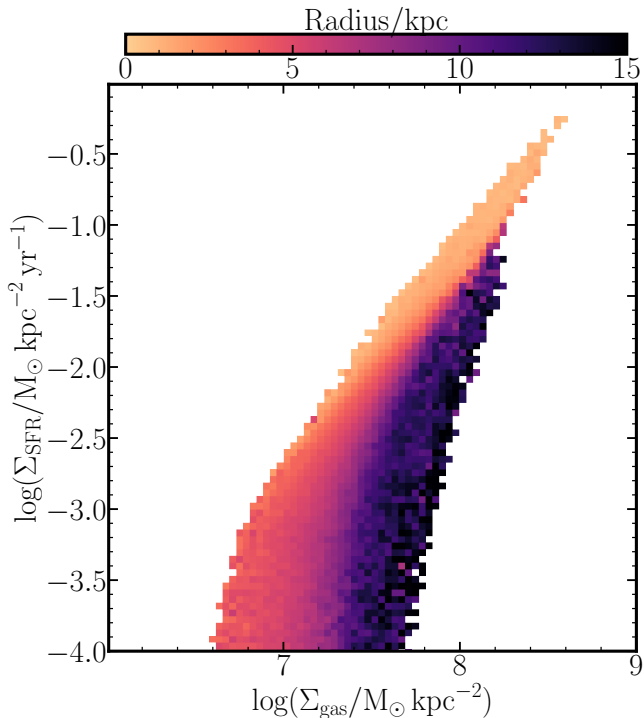


Figure 10. Radial dependence of the SK relation. The SK (same as Figure 8) colored coded by the average galactocentric distance of spaxels.

main sequence opposed to a *molecular* gas mass main sequence. Recent observational work has shown that the molecular gas content of galaxies is what is driving the existence of the rSFMS (Lin et al. 2019; Morselli et al. 2020; Baker et al. 2022, 2023b; Ellison et al. 2024)⁶. The molecular gas content of galaxies is likely more tightly correlated with the ongoing SFR than the overall gas fraction since star formation occurs within giant molecular clouds. The TNG model, however, does not explicitly track the individual phases (i.e., atomic, neutral, and molecular) of gas. Efforts have been made to recover the different phases of the gas in post-processing (see, e.g., Diemer et al. 2018, 2019); regardless, we leave the detailed examinations of the individual phases of the gas for future work.

4.1.1. On the Mass Dependence of the rSFMS

One counter-intuitive point to the above argument is that both the median SK relation and $f_{\text{gas}}-\Sigma_{\star}$ relation show very little dependence on host galaxies’ stellar masses. It should follow, then, that the rSFMS would not depend on host galaxies’ stellar masses either, since

⁶ Moreover, Ellison et al. (2024) show that the dynamical equilibrium pressure of systems is even more fundamental in driving the rSFMS.

the rSFMS is a combination of the two relations. Yet, there is some interesting, stellar mass dependent behavior hidden within the rSFMS (see Section 3.1.2, Figure 4). In this section, we argue that the dependence of rSFMS on host galaxies’ stellar masses comes from the combination of the SK relation and radially decreasing Σ_{\star} profiles.

Figure 10 shows the SK relation color-coded by the average galactocentric distance within each (histogram) pixel. There is a clear trend in the scatter of spaxels with distance to their galactic centers. For spaxels with the same Σ_{gas} , spaxels closer to their galactic center tend to have a higher Σ_{SFR} . Clearly, this shift in the normalization of SK relation with spaxels’ radii indicates a change in the star formation efficiency for spaxels at different locations within the galaxies. For regions near the galactic center, gases are more compressed vertically compared with regions further away, since they sit deeper in the potential well of the dark matter halo. Even with the same Σ_{gas} , those central regions have a higher physical gas density ρ_{gas} and, consequently, a higher star formation efficiency. Moreover, the spaxels with large values of Σ_{\star} tend to be closer to their galactic centers, which is unsurprising based on the radially-declining Σ_{\star} profiles in TNG (Wang et al. 2018; Wang & Lilly 2023). We also note that the range of galactocentric distances depends on stellar mass: more massive galaxies are larger, and thus their spaxels span a wider range of distances from their respective centers (see, e.g., Genel et al. 2018).

Figure 11 shows the rSFMS broken into the four different mass bins and color-coded by the spaxel’s galactocentric distance. We find that spaxels which belong to less massive galaxies tend to be closer to the center of their host than spaxels of more massive galaxies at a fixed Σ_{\star} . As discussed in the previous section, the regions which are closer to the center of the galaxy preferentially live in the upper right of the SK relation (i.e., high gas mass, high SFR; Figure 10). Therefore, for a fixed Σ_{\star} , lower mass galaxies tend to have spaxels which are more star-forming than their high (total) mass counterparts. This makes the rSFMS steeper for less massive galaxies than for more massive galaxies (seen both in Figures 4 and 11 and Table 1). The dependence of rSFMS on host galaxies’ stellar masses is therefore a consequence of changing star formation efficiency at different galactocentric distances for sub-galactic regions.

4.2. A Generalized Resolved Leaky-Box Model

On global scales, closed box and/or leaky box (also referred to as bathtub) models have been employed to interpret the observed scaling relations (see, e.g., Finlator & Davé 2008; Lilly et al. 2013; Forbes et al. 2014).

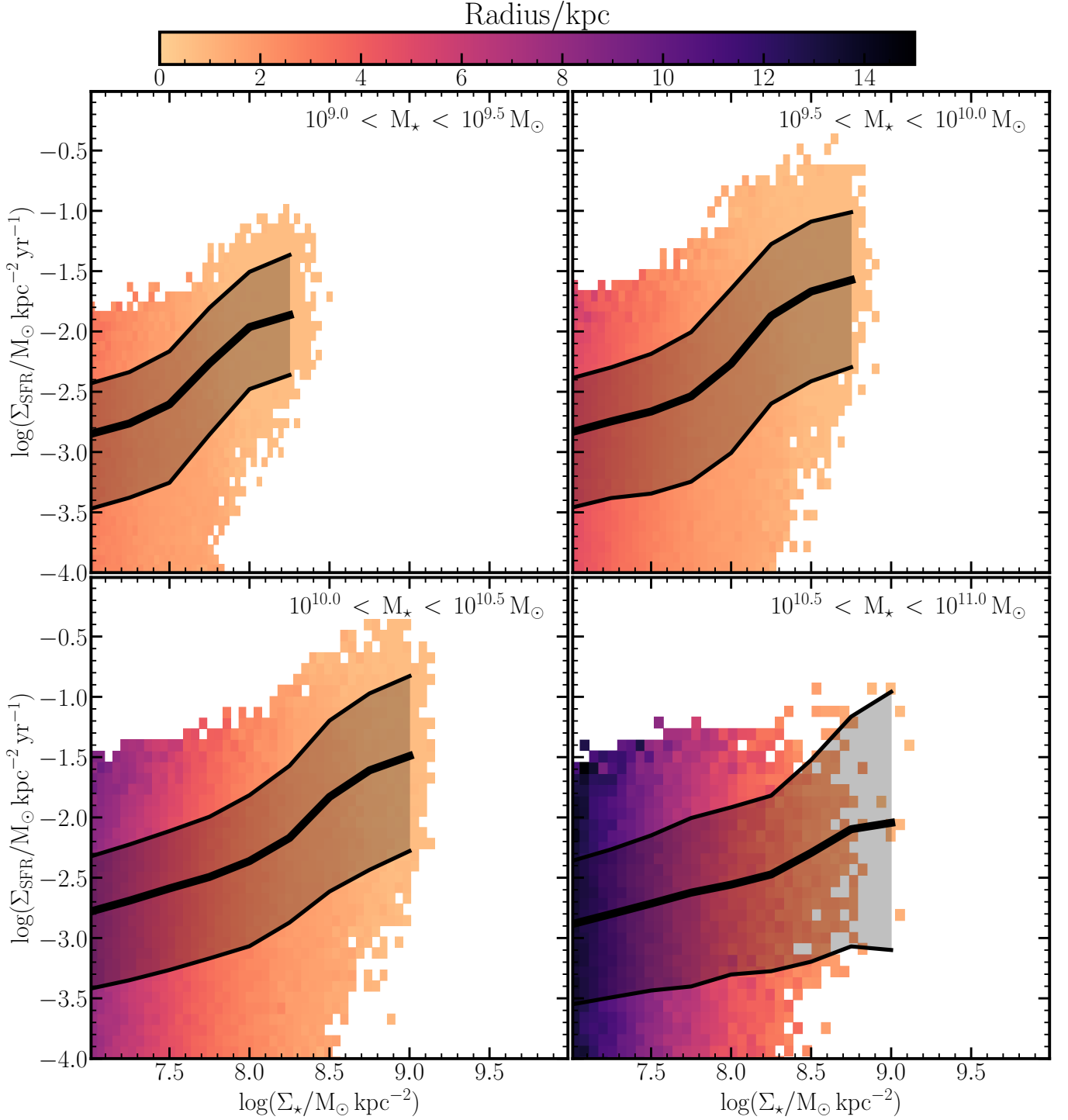


Figure 11. The radial dependence of the rSFMS. Same as Figure 4, but now binned by total stellar mass of the host galaxy (top-left is $10^{9.0} < M_{\star}/M_{\odot} < 10^{9.5}$, top-right is $10^{9.5} < M_{\star}/M_{\odot} < 10^{10.0}$, bottom-left is $10^{10.0} < M_{\star}/M_{\odot} < 10^{10.5}$, and bottom-right is $10^{10.5} < M_{\odot} < 10^{11.0}$). Additionally, each panel is color-coded by the average galactocentric radius of the spaxels.

Yet there has been comparatively little done on resolved scales. One such work, by [Zhu et al. \(2017\)](#), designs a resolved leaky-box model to describe the evolution of the Σ_\star , Σ_{gas} , and gas-phase metallicity at the spaxel level. The [Zhu et al. \(2017\)](#) model successfully predicts a tight rMZR, in line with the observed relation from IFS surveys (see, e.g., [Sánchez et al. 2013](#); [Barrera-Ballesteros et al. 2016](#)). Inspired by these results, we modify and expand this resolved leaky box model to include the $\Sigma_{\text{gas}} - \Sigma_\star$ relation as well as explicit inflow and outflow terms.

We take a rectangular prism through a $1 \text{ kpc} \times 1 \text{ kpc}$ patch of the galaxy to represent an “observed” spaxel. The evolution of this spaxel can be quantified in terms of its components: (i) stellar mass surface density $\Sigma_\star(t)$, (ii) gas mass surface density $\Sigma_{\text{gas}}(t)$, (iii) SFR surface density $\Sigma_{\text{SFR}}(t)$, and (iv) local gas-phase metallicity $Z(t)$.

We begin with the evolution of stellar mass surface density. To first order, the stellar mass content within our spaxel will be governed by the competition of new star formation and the death of old stars. This can be expressed as

$$\frac{d\Sigma_\star}{dt} = (1 - \mathcal{R})\Sigma_{\text{SFR}}(t) , \quad (5)$$

where \mathcal{R} denotes the fraction of stellar mass that is returned to the ISM from short-lived massive stars. In more detail, there should also be some term that describes the radial migration of stars into and out of the spaxel. However, we assume that the average stellar mass migration is negligible (see [Gurvich et al. 2020](#)).

We next consider the evolution of the gas content of our spaxel. Similar to the stellar component, the gas is driven by consumption (new star formation) and enrichment (mass return from stars). The gas mass is therefore, in a closed system, governed in a very similar way to Equation 5 (albeit with an opposite sign):

$$\frac{d\Sigma_{\text{gas}}}{dt} = -(1 - \mathcal{R})\Sigma_{\text{SFR}}(t) . \quad (6)$$

To extend Equation 6 to a leaky-box model, we must consider gas exchange with neighbouring spaxels. In principle, gas can advect across the boundaries of the rectangular prism in a number of different ways. The TNG model specifically implements gas outflows in the form of winds, whose strength is related to the SFR ([Springel & Hernquist 2003](#)). We can therefore write the surface density of outflowing gas as

$$\frac{d\Sigma_{\text{gas, out}}}{dt} = -\eta_{\text{out}}\Sigma_{\text{SFR}}(t) , \quad (7)$$

where η_{out} is the outflow mass loading factor of these winds. Similarly, previous studies suggest that the in-

flow rate is proportional to the SFR on galactic scales ([Toyouchi & Chiba 2015](#)). We therefore make the (crude) assumption that this proportionality holds down to the sub-galactic scales such that the surface density of inflowing gas can be expressed as

$$\frac{d\Sigma_{\text{gas, in}}}{dt} = \eta_{\text{in}}\Sigma_{\text{SFR}}(t) , \quad (8)$$

where η_{in} is the inflow mass loading factor of the winds. Combining Equations 6-8, the complete description of the gas evolution is given by

$$\frac{d\Sigma_{\text{gas}}}{dt} = -(1 - \mathcal{R} - \eta_{\text{in}} + \eta_{\text{out}})\Sigma_{\text{SFR}}(t) . \quad (9)$$

Recall, however, that Σ_{SFR} is a function of Σ_{gas} via the SK relation (Equation 2) so that

$$\frac{d\Sigma_{\text{gas}}}{dt} = -\epsilon(1 - \mathcal{R} - \eta_{\text{in}} + \eta_{\text{out}})\Sigma_{\text{gas}}^k(t) . \quad (10)$$

Although Eqn. 10 is a non-linear differential equation, if $k > 1$ (as in the case for the SK relation), we can express its solution analytically:

$$\Sigma_{\text{gas}}(t) = (\Sigma_{\text{gas}, 0}^{1-k} - (1 - k)(1 - \mathcal{R} - \eta_{\text{in}} + \eta_{\text{out}})\epsilon t)^{\frac{1}{1-k}} . \quad (11)$$

Indeed, Equation 11 is a generalization of Equation 6 of [Zhu et al. \(2017\)](#) with explicit inflow and outflow terms.

Finally, to model the local metallicity evolution, $Z(t)$, in each spaxel, we introduce $\Sigma_{\text{metal}}(t)$ the surface density of gas-phase metals such that

$$\Sigma_{\text{metal}}(t) = Z(t)\Sigma_{\text{gas}} , \quad (12)$$

which implies that

$$\frac{dZ}{dt} = \frac{1}{\Sigma_{\text{gas}}} \left[\frac{d\Sigma_{\text{metal}}}{dt} - Z(t)\frac{d\Sigma_{\text{gas}}}{dt} \right] , \quad (13)$$

via the quotient rule of derivatives. There are four channels through which amount of gas-phase metals in a spaxel can be altered. In the closed box, metals can either be consumed through star formation

$$\frac{d\Sigma_{\text{metal, consume}}}{dt} = -Z(t)\Sigma_{\text{SFR}}(t) , \quad (14)$$

or stars (which generate new metals) can enrich the ISM,

$$\frac{d\Sigma_{\text{metal, enrich}}}{dt} = y\Sigma_{\text{SFR}}(t) , \quad (15)$$

where y is the metal yield from the stars. Extending this to a leaky-box, gas inflows can bring in metals from the circumgalactic medium, intergalactic medium and/or, from neighboring spaxels,

$$\frac{d\Sigma_{\text{metal, in}}}{dt} = Z_{\text{in}}\frac{d\Sigma_{\text{gas, in}}}{dt} = Z_{\text{in}}\eta_{\text{in}}\Sigma_{\text{SFR}} , \quad (16)$$

where Z_{in} denotes metallicity of the inflowing gas. Gas (with the same metallicity of the spaxel) can also be launched from the spaxel via winds

$$\begin{aligned} \frac{d\Sigma_{\text{metal, out}}}{dt} &= Z(t) \frac{d\Sigma_{\text{gas, out}}}{dt} + \Sigma_{\text{gas, out}}(t) \frac{dZ}{dt} \\ &= -Z(t)\eta_{\text{out}}\Sigma_{\text{SFR}} + \Sigma_{\text{gas, out}}(t) \frac{dZ}{dt}. \end{aligned} \quad (17)$$

Combining Equations 14-17, the evolution of Σ_{metal} is described by

$$\begin{aligned} \frac{d\Sigma_{\text{metal}}}{dt} &= [y - Z(t) + Z_{\text{in}}\eta_{\text{in}} - Z(t)\eta_{\text{out}}]\Sigma_{\text{SFR}}(t) \\ &\quad + \Sigma_{\text{gas, out}}(t) \frac{dZ}{dt}. \end{aligned} \quad (18)$$

Plugging in Equations 9 and 18 into Equation 13 we obtain an analytic expression for the evolution of the local metallicity

$$\frac{dZ}{dt} = \frac{\Sigma_{\text{SFR}}(t)}{\Sigma_{\text{gas}}(t) - \Sigma_{\text{gas, out}}(t)} \left(y - Z(t)\mathcal{R} + \eta_{\text{in}}[Z_{\text{in}} - Z(t)] \right). \quad (19)$$

Equation 19 contains three “terms” representing the physics driving the metallicity evolution. The first term is the coefficient outside the parentheses. This coefficient represents a “gas consumption timescale”: it is the rate at which gas is turning into stars divided by the total amount of gas left in the spaxel after an outflow event. If the local SFR increases (or the spaxel undergoes a large outflow event), the rate of change of metallicity will also increase. The terms in the parentheses of Equation 19 represent contributions from the closed and leaky boxes. The closed box term is $y - Z(t)\mathcal{R}$. In plain terms, if the stars return more metals into the ISM, the spaxel will increase its metallicity faster. The second regime is that when the spaxel is already metal rich its metallicity will change more slowly. Combined, the yield and return suggest that, in the limit of no exchange from one spaxel to another, the system will be entirely dominated by new star formation and prior enrichment. The leaky-box term is $\eta_{\text{in}}[Z_{\text{in}} - Z(t)]$. This represents a dilution term from the inflowing material: as the difference between the inflowing metallicity and current metallicity increases, so too does the overall rate of change of the metallicity (scaled by the mass loading factors). In the limit of no new star formation or return from stars to the ISM, the change in the spaxel’s metallicity will be dominated by inflowing material. Notably, Equation 19 does not depend on the outflows from the spaxel beyond decreasing the gas reservoir for future star formation.

Equations 5, 10, and 19 give the full set of differential equations that regulate the evolution of a spaxel. Before

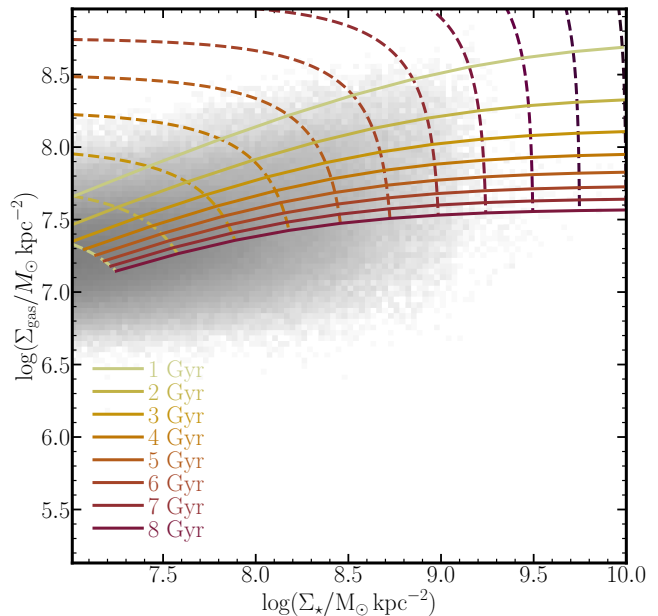


Figure 12. The gas mass main sequence in a resolved closed-box model. evolution of simulated closed boxes on the MZR plane. The colored background display our IllustrisTNG spaxels. The dashed lines track the evolution of individual closed-boxed spaxels. The colored-solid lines our close-box predictions at various times, as labeled.

proceeding, there are a few model parameters we adopt based on the TNG model. TNG assumes no primordial stars and metals, so that $\Sigma_{\star}(0) = 0$ and $Z(0) = 0$. The initial gas mass surface density, however, we leave as a free parameter using values ranging from $10^{7.5}$ to $10^{10.0} M_{\odot} \text{ kpc}^{-2}$ in steps of 0.25 dex. Additionally, we assume that the inflowing metallicity at any given time is pristine ($Z_{\text{in}} = 0$) from the intergalactic medium⁷. The return fraction, \mathcal{R} , can be estimated as $\mathcal{R} = 0.5$ by integrating the Chabrier (2003; which TNG uses) initial mass function. We take k and ϵ of the SK relation from the best fit in Section 4.1. Finally, the average metal yield from stars in TNG is $y = 0.05$ (Torrey et al. 2019).

4.2.1. Fiducial Closed Box Model

We begin by examining our toy model using a closed box assumption where $\eta_{\text{in}} = \eta_{\text{out}} = 0.0$. We numerically integrate Equations 5, 10, and 19 given the initial conditions set forth in the previous section.

⁷ In reality, inflows can be pre-enriched recycled gas from the circumgalactic medium, metal rich flows from neighboring spaxels, or non-zero metallicity gas from anywhere in the environment. The effect of a non-zero Z_{in} would be to decrease dZ/dt (from the dilution term of equation 19). Moreover, if $Z_{\text{in}} > Z(t)$ (i.e., very metal rich inflows), the sign of the dilution term will change, but the overall behavior of the model will be largely the same as $Z_{\text{in}} < Z(t)$.

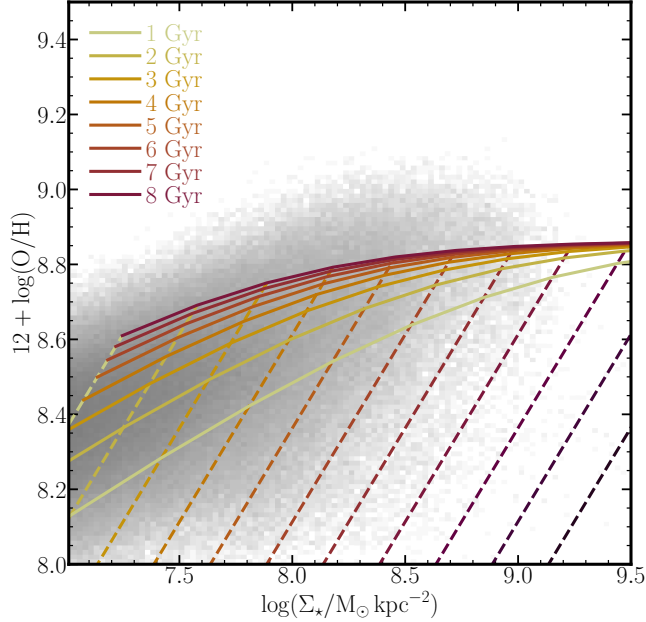


Figure 13. The rMZR in a resolved closed-box model. The colored background shows the distribution of simulated TNG spaxels. The dashed lines track the evolution of representative individual spaxels. The solid lines represent the rMZR predictions in our closed-box model.

Figure 12 shows $\Sigma_{\text{gas}}-\Sigma_{\star}$ relation against our resolved leaky-box model. The solid lines connect the position of different leaky-box spaxels at a fixed integration time, whereas the colored-dash lines track the gas-fraction evolution for a fixed initial Σ_{gas} values. The shape of the dashed lines indicate the connection between gas consumption and stellar growth. We note that, after 1 Gyr of evolution (lightest blue), our leaky-box prediction reaches the upper envelope of our 2D distribution drawn from TNG – and after ~ 3 -4 Gyrs, the model lands on the local relation. The median $\Sigma_{\text{gas}} - \Sigma_{\star}$ relation (shown in the thick solid red line) of TNG starts to emerge as the evolution continues. Moreover, past $t \gtrsim 5$ Gyr the behavior of our model becomes asymptotic, modest changes in the length of the integration time have only modest changes in the gas fractions.

Figure 13 shows our closed box model predictions for the rMZR. The solid lines again indicate spaxel locations in the rMZR at times $t > t_0$ and the dashed lines depict the same five representative spaxel tracks displayed in Figure 12. As time progresses, a given spaxel grows its stellar component – and it becomes more metal-rich, as gas recently locked in short-lived stars is returned to the ISM. After 1 Gyr of evolution, our prediction lies on the lower envelope of the TNG relation, reaching the local relation after ~ 2 -3 Gyr, noting that the closed box model assumptions made here seem to overpredict the

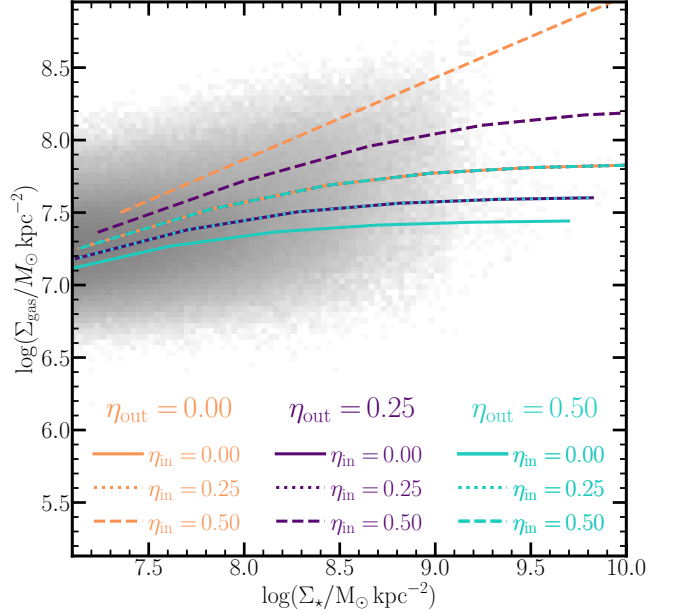


Figure 14. The gas mass main sequence in a resolved leaky-box model. The $f_{\text{gas}}-\Sigma_{\star}$ formed with different choices of η_{in} and η_{out} . The colored background shows the distribution of actual IllustrisTNG spaxels included in this study. The colored-solid lines are the relations formed by spaxels at $t = 5$ Gyr under different model assumptions, as labeled.

median rMZR past ~ 3 Gyr. Similar to the behavior of the $\Sigma_{\text{gas}} - \Sigma_{\star}$ relation, past $t \gtrsim 5$ Gyr the behavior of this model is asymptotic.

4.2.2. Inflow/Outflow Variations

To explore how different inflow/outflow models affect the results for resolved scaling relations, we run the same leaky-box model with different mass-loading factors for inflows and outflows, namely, a combination of $\eta_{\text{in}} = \{0.0, 0.25, 0.5\}$ and $\eta_{\text{out}} = \{0.0, 0.25, 0.5\}$. The choice of upper bound value 0.5 for our mass-loading factor variation is because we adopt a stellar return fraction $\mathcal{R} = 0.5$ and any inflow with $\eta_{\text{in}} > 0.5$ will become a runaway process. Figure 14 and 15 show predictions for rSFMS and rMZR from our resolved leaky-box model at $t = 5$ Gyrs, after which the evolution of resolved scaling relations in our model becomes asymptotic, with different combinations of η_{in} and η_{out} values. The leaky-box $f_{\text{gas}} - \Sigma_{\star}$ prediction relies on the net outflow. If the net outflow is negative, in other words, a net inflow, the spaxels' gas fraction becomes too high compared to what we observe for TNG spaxels. The supply of inflow gas maintains the gas fraction, and consequently, the SFR at high levels. To be consistent with the result for $f_{\text{gas}} - \Sigma_{\star}$ relation we observe in TNG, a positive, or near zero, net outflow is preferred.

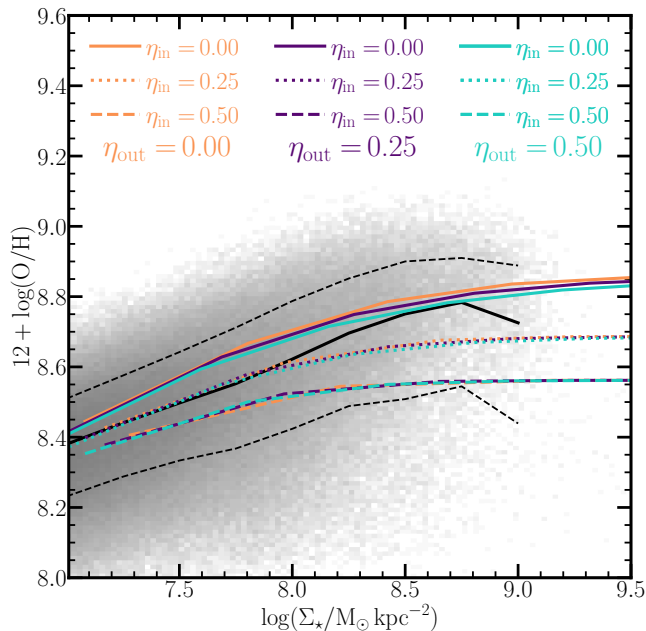


Figure 15. The rMZR in a resolved leaky-box model. The rMZR formed with different choices of η_{in} and η_{out} . The colored background shows the distribution of actual IllustrisTNG spaxels included in this study, the same as Figure 5. The colored-solid lines are the relations formed by spaxels at $t = 5$ Gyr under different model assumptions, as labeled.

On the other hand, the rMZR does not display dependence on the net inflow/outflow rate. Instead, models are affected by only the inflow factor η_{in} : the higher the η_{in} is, the lower normalization and shallower slope the predicted rMZR has. This is because metallicity will be significantly diluted with the inflow of primordial gas, which has zero metallicity. At fixed η_{in} , the predicted rMZR is insensitive to the adopted outflow strength η_{out} . This, obviously, stems from our assumption that the outflowing metallicity is the same as the current metallicity; therefore, the overall ratio of metal mass to total mass remains unchanged from outflows (see Equation 19). If the metallicity of the outflows were preferentially metal poor or metal rich, however, there would likely be an impact of the overall metal evolution of spaxels. Regardless, resolved leaky-box models (e.g., Zhu et al. 2017) that invoke ‘net’ outflow rates (without a distinct inflow rate) do not sufficiently capture the behavior of the rMZR.

5. SUMMARY

We have studied the spatially resolved scaling relations between physical properties for star-forming galaxies at $z = 0$ in IllustrisTNG. We selected star-forming galaxies from an IllustrisTNG snapshot and produce spatially resolved property maps for them (see Figure 1).

We then present the two scaling relations, the resolved star-formation main sequence (rSFMS) and the resolved mass-metallicity relation (rMZR), compare them with results from observational surveys, and discuss the tightness and residual of the rSFMS. Our conclusions are as follows,

- (i) The rSFMS exists within IllustrisTNG galaxies, as a positive single-power-law correlation between the stellar mass surface density Σ_* and the star formation rate surface density Σ_{SFR} at the scale of 1 kpc^2 (Figure 2). The rSFMS has a slope of 0.6, and a 1σ scatter of 0.6 dex. The rSFMS from our results agrees well with IFU observations in both shape and normalization.
- (ii) We find that the rSFMS exhibits changes in both slope and normalization across galaxies with different total stellar masses (Figures 3 and 4).
- (iii) The gas-phase metallicity is positively correlated with Σ_{SFR} (Figure 5). The rMZR within IllustrisTNG galaxies qualitatively agrees with the similar metallicity relation from IFU observations (though we caution against too strong a comparison; see discussion in Section 3.2). In particular, the rMZR in IllustrisTNG successfully recreates the characteristic features of a single-power-law in the low mass regime and a plateau in the high mass regime. The rMZR shows small variations for different host galaxies.
- (iv) We investigate the scatter about the rMZR and find that it is positively correlated with Σ_{SFR} (Figure 6), which is the *opposite* trend at the global MZR. Moreover, we find that the rMZR is virtually independent of galaxy host mass (Figure 7).
- (v) We investigate the origin of the rSFMS by considering the Schmidt-Kennicutt relation and gas mass main sequence ($\Sigma_{\text{gas}}-\Sigma_*$ relation) in TNG (Figures 8 and 9, respectively). The combination of these two scaling relations can naturally explain the emergence of the rSFMS in TNG. Moreover, we suggest that the mass dependence of the rSFMS lies within the radial dependence of these relations (Figures 10 and 11).
- (vi) Finally, we show that gas mass main sequence and rMZR for IllustrisTNG regions can be well described by a generalization of the leaky-box model of Zhu et al. (2017; see Figures 12-15). The gas mass main sequence depends on both the inflow and outflow mass loading factors, whereas the rMZR only exhibits a strong dependence on the inflowing mass

loading factor. Overall the leaky-box model indicates that the resolved galaxy scaling relations in IllustrisTNG are governed by feedback on the local scales (~ 1 kpc) of the galaxy.

Fundamentally, star formation and chemical enrichment are “local” processes within galaxies. Understanding and quantifying the extent to which simulation models – which nominally reproduce realistic galaxy populations on integrated scales – agree/disagree with observa-

tions on these scales can be a critical test of their sub-grid prescriptions. Current and future IFS campaigns promise to shed light in this area and give us a deeper understanding of what drives galaxy’s evolution on sub-galactic scales.

- 1 AMG and PT acknowledge support from NSF-AST
- 2 2346977.

REFERENCES

- Abdurro’uf, & Akiyama, M. 2019, arXiv e-prints.
<https://arxiv.org/abs/1902.07712>
- Andrews, B. H., & Martini, P. 2013, *ApJ*, 765, 140,
 doi: [10.1088/0004-637X/765/2/140](https://doi.org/10.1088/0004-637X/765/2/140)
- Baker, W. M., Maiolino, R., Bluck, A. F. L., et al. 2022,
MNRAS, 510, 3622, doi: [10.1093/mnras/stab3672](https://doi.org/10.1093/mnras/stab3672)
- Baker, W. M., Maiolino, R., Belfiore, F., et al. 2023a,
MNRAS, 519, 1149, doi: [10.1093/mnras/stac3594](https://doi.org/10.1093/mnras/stac3594)
- . 2023b, *MNRAS*, 518, 4767,
 doi: [10.1093/mnras/stac3413](https://doi.org/10.1093/mnras/stac3413)
- Barrera-Ballesteros, J. K., Sánchez, S. F., Heckman, T.,
 Blanc, G. A., & MaNGA Team. 2017, *ApJ*, 844, 80,
 doi: [10.3847/1538-4357/aa7aa9](https://doi.org/10.3847/1538-4357/aa7aa9)
- Barrera-Ballesteros, J. K., Heckman, T. M., Zhu, G. B.,
 et al. 2016, *Monthly Notices of the Royal Astronomical
 Society*, 463, 2513, doi: [10.1093/mnras/stw1984](https://doi.org/10.1093/mnras/stw1984)
- Barrera-Ballesteros, J. K., Heckman, T., Sánchez, S. F.,
 et al. 2018, *ApJ*, 852, 74, doi: [10.3847/1538-4357/aa9b31](https://doi.org/10.3847/1538-4357/aa9b31)
- Belli, S., Jones, T., Ellis, R. S., & Richard, J. 2013, *ApJ*,
 772, 141, doi: [10.1088/0004-637X/772/2/141](https://doi.org/10.1088/0004-637X/772/2/141)
- Berg, D. A., Skillman, E. D., Marble, A. R., et al. 2012,
ApJ, 754, 98, doi: [10.1088/0004-637X/754/2/98](https://doi.org/10.1088/0004-637X/754/2/98)
- Blanc, G. A., Lu, Y., Benson, A., Katsianis, A., & Barraza,
 M. 2019, *ApJ*, 877, 6, doi: [10.3847/1538-4357/ab16ec](https://doi.org/10.3847/1538-4357/ab16ec)
- Bolatto, A. D., Wong, T., Utomo, D., et al. 2017, *ApJ*, 846,
 159, doi: [10.3847/1538-4357/aa86aa](https://doi.org/10.3847/1538-4357/aa86aa)
- Brinchmann, J., Charlot, S., White, S. D. M., et al. 2004,
MNRAS, 351, 1151,
 doi: [10.1111/j.1365-2966.2004.07881.x](https://doi.org/10.1111/j.1365-2966.2004.07881.x)
- Brown, T., Roberts, I. D., Thorp, M., et al. 2023a, *ApJ*,
 956, 37, doi: [10.3847/1538-4357/acf195](https://doi.org/10.3847/1538-4357/acf195)
- Brown, W., Patton, D. R., Ellison, S. L., & Faria, L. 2023b,
MNRAS, 522, 5107, doi: [10.1093/mnras/stad1314](https://doi.org/10.1093/mnras/stad1314)
- Bryant, J. J., Owers, M. S., Robotham, A. S. G., et al.
 2015, *MNRAS*, 447, 2857, doi: [10.1093/mnras/stu2635](https://doi.org/10.1093/mnras/stu2635)
- Bundy, K., Bershadsky, M. A., Law, D. R., et al. 2015, *ApJ*,
 798, 7, doi: [10.1088/0004-637X/798/1/7](https://doi.org/10.1088/0004-637X/798/1/7)
- Cano-Díaz, M., Ávila-Reese, V., Sánchez, S. F., et al. 2019,
MNRAS, 488, 3929, doi: [10.1093/mnras/stz1894](https://doi.org/10.1093/mnras/stz1894)
- Cano-Díaz, M., Sánchez, S. F., Zibetti, S., et al. 2016,
ApJL, 821, L26, doi: [10.3847/2041-8205/821/2/L26](https://doi.org/10.3847/2041-8205/821/2/L26)
- Chabrier, G. 2003, *PASP*, 115, 763, doi: [10.1086/376392](https://doi.org/10.1086/376392)
- Daddi, E., Dickinson, M., Morrison, G., et al. 2007, *ApJ*,
 670, 156, doi: [10.1086/521818](https://doi.org/10.1086/521818)
- Davé, R., Finlator, K., & Oppenheimer, B. D. 2011,
MNRAS, 416, 1354,
 doi: [10.1111/j.1365-2966.2011.19132.x](https://doi.org/10.1111/j.1365-2966.2011.19132.x)
- Davis, M., Efstathiou, G., Frenk, C. S., & White, S. D. M.
 1985, *ApJ*, 292, 371, doi: [10.1086/163168](https://doi.org/10.1086/163168)
- De Rossi, M. E., Theuns, T., Font, A. S., & McCarthy, I. G.
 2015, *MNRAS*, 452, 486, doi: [10.1093/mnras/stv1287](https://doi.org/10.1093/mnras/stv1287)
- Diemer, B., Stevens, A. R. H., Forbes, J. C., et al. 2018,
ApJS, 238, 33, doi: [10.3847/1538-4365/aae387](https://doi.org/10.3847/1538-4365/aae387)
- Diemer, B., Stevens, A. R. H., Lagos, C. d. P., et al. 2019,
MNRAS, 487, 1529, doi: [10.1093/mnras/stz1323](https://doi.org/10.1093/mnras/stz1323)
- Doherty, C. L., Gil-Pons, P., Lau, H. H. B., Lattanzio,
 J. C., & Siess, L. 2014, *MNRAS*, 437, 195,
 doi: [10.1093/mnras/stt1877](https://doi.org/10.1093/mnras/stt1877)
- Donnari, M., Pillepich, A., Nelson, D., et al. 2019, *MNRAS*,
 485, 4817, doi: [10.1093/mnras/stz712](https://doi.org/10.1093/mnras/stz712)
- Elbaz, D., Daddi, E., Le Borgne, D., et al. 2007, *A&A*, 468,
 33, doi: [10.1051/0004-6361:20077525](https://doi.org/10.1051/0004-6361:20077525)
- Ellison, S. L., Lin, L., Thorp, M. D., et al. 2021, *MNRAS*,
 501, 4777, doi: [10.1093/mnras/staa3822](https://doi.org/10.1093/mnras/staa3822)
- Ellison, S. L., Patton, D. R., Simard, L., & McConnachie,
 A. W. 2008, *ApJL*, 672, L107, doi: [10.1086/527296](https://doi.org/10.1086/527296)
- Ellison, S. L., Sánchez, S. F., Ibarra-Medel, H., et al. 2018,
MNRAS, 474, 2039, doi: [10.1093/mnras/stx2882](https://doi.org/10.1093/mnras/stx2882)
- Ellison, S. L., Thorp, M. D., Lin, L., et al. 2020, *MNRAS*,
 493, L39, doi: [10.1093/mnrasl/slz179](https://doi.org/10.1093/mnrasl/slz179)
- Ellison, S. L., Pan, H.-A., Bluck, A. F. L., et al. 2024,
MNRAS, 527, 10201, doi: [10.1093/mnras/stad3778](https://doi.org/10.1093/mnras/stad3778)
- Elmegreen, B. G. 1999, *ApJ*, 527, 266, doi: [10.1086/308073](https://doi.org/10.1086/308073)
- Enia, A., Rodighiero, G., Morselli, L., et al. 2020, *MNRAS*,
 493, 4107, doi: [10.1093/mnras/staa433](https://doi.org/10.1093/mnras/staa433)

- Erroz-Ferrer, S., Carollo, C. M., den Brok, M., et al. 2019, *MNRAS*, 484, 5009, doi: [10.1093/mnras/stz194](https://doi.org/10.1093/mnras/stz194)
- Faber, S. M., & Jackson, R. E. 1976, *ApJ*, 204, 668, doi: [10.1086/154215](https://doi.org/10.1086/154215)
- Finlator, K., & Davé, R. 2008, *MNRAS*, 385, 2181, doi: [10.1111/j.1365-2966.2008.12991.x](https://doi.org/10.1111/j.1365-2966.2008.12991.x)
- Fishlock, C. K., Karakas, A. I., Lugaro, M., & Yong, D. 2014, *ApJ*, 797, 44, doi: [10.1088/0004-637X/797/1/44](https://doi.org/10.1088/0004-637X/797/1/44)
- Forbes, J. C., Krumholz, M. R., Burkert, A., & Dekel, A. 2014, *MNRAS*, 443, 168, doi: [10.1093/mnras/stu1142](https://doi.org/10.1093/mnras/stu1142)
- Furlong, M., Bower, R. G., Theuns, T., et al. 2015, *MNRAS*, 450, 4486, doi: [10.1093/mnras/stv852](https://doi.org/10.1093/mnras/stv852)
- Gao, Y., Wang, E., Kong, X., et al. 2018, *ApJ*, 868, 89, doi: [10.3847/1538-4357/aae9f1](https://doi.org/10.3847/1538-4357/aae9f1)
- Garcia, A. M., Torrey, P., Hemler, Z. S., et al. 2023, *MNRAS*, 519, 4716, doi: [10.1093/mnras/stac3749](https://doi.org/10.1093/mnras/stac3749)
- Garcia, A. M., Torrey, P., Ellison, S. L., et al. 2024a, arXiv e-prints, arXiv:2407.06254, doi: [10.48550/arXiv.2407.06254](https://doi.org/10.48550/arXiv.2407.06254)
- Garcia, A. M., Torrey, P., Ellison, S., et al. 2024b, *MNRAS*, 531, 1398, doi: [10.1093/mnras/stae1252](https://doi.org/10.1093/mnras/stae1252)
- Genel, S., Nelson, D., Pillepich, A., et al. 2018, *MNRAS*, 474, 3976, doi: [10.1093/mnras/stx3078](https://doi.org/10.1093/mnras/stx3078)
- Gurvich, A. B., Faucher-Giguère, C.-A., Richings, A. J., et al. 2020, *MNRAS*, 498, 3664, doi: [10.1093/mnras/staa2578](https://doi.org/10.1093/mnras/staa2578)
- Hani, M. H., Hayward, C. C., Orr, M. E., et al. 2020, *MNRAS*, 493, L87, doi: [10.1093/mnrasl/slaa013](https://doi.org/10.1093/mnrasl/slaa013)
- Hemler, Z. S., Torrey, P., Qi, J., et al. 2021, *MNRAS*, 506, 3024, doi: [10.1093/mnras/stab1803](https://doi.org/10.1093/mnras/stab1803)
- Hemmati, S., Mobasher, B., Miller, S., & Nayyeri, H. 2014, in *American Astronomical Society Meeting Abstracts*, Vol. 223, American Astronomical Society Meeting Abstracts #223, 145.16
- Hsieh, B. C., Lin, L., Lin, J. H., et al. 2017, *ApJL*, 851, L24, doi: [10.3847/2041-8213/aa9d80](https://doi.org/10.3847/2041-8213/aa9d80)
- Hwang, H.-C., Barrera-Ballesteros, J. K., Heckman, T. M., et al. 2019, *ApJ*, 872, 144, doi: [10.3847/1538-4357/aaf7a3](https://doi.org/10.3847/1538-4357/aaf7a3)
- Ji, X., & Yan, R. 2022, *A&A*, 659, A112, doi: [10.1051/0004-6361/202142312](https://doi.org/10.1051/0004-6361/202142312)
- Karakas, A. I. 2010, *MNRAS*, 403, 1413, doi: [10.1111/j.1365-2966.2009.16198.x](https://doi.org/10.1111/j.1365-2966.2009.16198.x)
- Kennicutt, Robert C., J. 1998, *ApJ*, 498, 541, doi: [10.1086/305588](https://doi.org/10.1086/305588)
- Kewley, L. J., & Ellison, S. L. 2008, *ApJ*, 681, 1183, doi: [10.1086/587500](https://doi.org/10.1086/587500)
- Kewley, L. J., Nicholls, D. C., & Sutherland, R. S. 2019, *ARA&A*, 57, 511, doi: [10.1146/annurev-astro-081817-051832](https://doi.org/10.1146/annurev-astro-081817-051832)
- Kobayashi, C., Umeda, H., Nomoto, K., Tominaga, N., & Ohkubo, T. 2006, *ApJ*, 653, 1145, doi: [10.1086/508914](https://doi.org/10.1086/508914)
- Koeppen, J. 1994, *A&A*, 281, 26
- Koller, M., Ziegler, B., Ciocan, B. I., et al. 2024, *A&A*, 689, A315, doi: [10.1051/0004-6361/202450715](https://doi.org/10.1051/0004-6361/202450715)
- Koprowski, M. P., Wijesekera, J. V., Dunlop, J. S., et al. 2024, arXiv e-prints, arXiv:2403.06575, doi: [10.48550/arXiv.2403.06575](https://doi.org/10.48550/arXiv.2403.06575)
- Lacey, C. G., & Fall, S. M. 1985, *ApJ*, 290, 154, doi: [10.1086/162970](https://doi.org/10.1086/162970)
- Lara-López, M. A., Cepa, J., Bongiovanni, A., et al. 2010, *A&A*, 521, L53, doi: [10.1051/0004-6361/201014803](https://doi.org/10.1051/0004-6361/201014803)
- Lee, H., Skillman, E. D., Cannon, J. M., et al. 2006, *ApJ*, 647, 970, doi: [10.1086/505573](https://doi.org/10.1086/505573)
- Lee, N., Sanders, D. B., Casey, C. M., et al. 2015, *ApJ*, 801, 80, doi: [10.1088/0004-637X/801/2/80](https://doi.org/10.1088/0004-637X/801/2/80)
- Leroy, A. K., Schinnerer, E., Hughes, A., et al. 2021, *ApJS*, 257, 43, doi: [10.3847/1538-4365/ac17f3](https://doi.org/10.3847/1538-4365/ac17f3)
- Leslie, S. K., Schinnerer, E., Liu, D., et al. 2020, *ApJ*, 899, 58, doi: [10.3847/1538-4357/aba044](https://doi.org/10.3847/1538-4357/aba044)
- Li, H., Vogelsberger, M., Marinacci, F., Sales, L. V., & Torrey, P. 2020, *MNRAS*, 499, 5862, doi: [10.1093/mnras/staa3122](https://doi.org/10.1093/mnras/staa3122)
- Lilly, S. J., Carollo, C. M., Pipino, A., Renzini, A., & Peng, Y. 2013, *ApJ*, 772, 119, doi: [10.1088/0004-637X/772/2/119](https://doi.org/10.1088/0004-637X/772/2/119)
- Lin, L., Pan, H.-A., Ellison, S. L., et al. 2019, *ApJL*, 884, L33, doi: [10.3847/2041-8213/ab4815](https://doi.org/10.3847/2041-8213/ab4815)
- Liu, Q., Wang, E., Lin, Z., et al. 2018, *ApJ*, 857, 17, doi: [10.3847/1538-4357/aab3d5](https://doi.org/10.3847/1538-4357/aab3d5)
- Maiolino, R., & Mannucci, F. 2019, *A&A Rv*, 27, 3, doi: [10.1007/s00159-018-0112-2](https://doi.org/10.1007/s00159-018-0112-2)
- Mannucci, F., Cresci, G., Maiolino, R., Marconi, A., & Gnerucci, A. 2010, *MNRAS*, 408, 2115, doi: [10.1111/j.1365-2966.2010.17291.x](https://doi.org/10.1111/j.1365-2966.2010.17291.x)
- Maragkoudakis, A. 2017, in *Linking Observations and Theory Across the Scales of Star Formation in Galaxies*, 9
- Marinacci, F., Vogelsberger, M., Pakmor, R., et al. 2018, *MNRAS*, 480, 5113, doi: [10.1093/mnras/sty2206](https://doi.org/10.1093/mnras/sty2206)
- McDonough, B., Curtis, O., & Brainerd, T. G. 2023, *ApJ*, 958, 19, doi: [10.3847/1538-4357/acfe0b](https://doi.org/10.3847/1538-4357/acfe0b)
- Medling, A. M., Cortese, L., Croom, S. M., et al. 2018, *MNRAS*, 475, 5194, doi: [10.1093/mnras/sty127](https://doi.org/10.1093/mnras/sty127)
- Moreno, J., Torrey, P., Ellison, S. L., et al. 2021, *MNRAS*, 503, 3113, doi: [10.1093/mnras/staa2952](https://doi.org/10.1093/mnras/staa2952)
- Morselli, L., Rodighiero, G., Enia, A., et al. 2020, *MNRAS*, 496, 4606, doi: [10.1093/mnras/staa1811](https://doi.org/10.1093/mnras/staa1811)
- Motwani, B., Genel, S., Bryan, G. L., et al. 2022, *ApJ*, 926, 139, doi: [10.3847/1538-4357/ac3d2d](https://doi.org/10.3847/1538-4357/ac3d2d)

- Naiman, J. P., Pillepich, A., Springel, V., et al. 2018, *MNRAS*, 477, 1206, doi: [10.1093/mnras/sty618](https://doi.org/10.1093/mnras/sty618)
- Nelson, D., Pillepich, A., Springel, V., et al. 2018, *MNRAS*, 475, 624, doi: [10.1093/mnras/stx3040](https://doi.org/10.1093/mnras/stx3040)
- Nelson, D., Springel, V., Pillepich, A., et al. 2019a, *Computational Astrophysics and Cosmology*, 6, 2, doi: [10.1186/s40668-019-0028-x](https://doi.org/10.1186/s40668-019-0028-x)
- Nelson, D., Pillepich, A., Springel, V., et al. 2019b, *MNRAS*, 490, 3234, doi: [10.1093/mnras/stz2306](https://doi.org/10.1093/mnras/stz2306)
- Nelson, E. J., Tacchella, S., Diemer, B., et al. 2021, *MNRAS*, 508, 219, doi: [10.1093/mnras/stab2131](https://doi.org/10.1093/mnras/stab2131)
- Nobels, F. S. J., Schaye, J., Schaller, M., et al. 2024, *MNRAS*, 532, 3299, doi: [10.1093/mnras/stae1390](https://doi.org/10.1093/mnras/stae1390)
- Noeske, K. G., Weiner, B. J., Faber, S. M., et al. 2007, *ApJL*, 660, L43, doi: [10.1086/517926](https://doi.org/10.1086/517926)
- Nomoto, K., Iwamoto, K., Nakasato, N., et al. 1997, *NuPhA*, 621, 467, doi: [10.1016/S0375-9474\(97\)00291-1](https://doi.org/10.1016/S0375-9474(97)00291-1)
- Orr, M., & Hopkins, P. 2019, in *American Astronomical Society Meeting Abstracts*, Vol. 233, American Astronomical Society Meeting Abstracts #233, 108.02
- Pan, H.-A., Lin, L., Hsieh, B.-C., et al. 2019, *ApJ*, 881, 119, doi: [10.3847/1538-4357/ab311c](https://doi.org/10.3847/1538-4357/ab311c)
- Patrício, V., Richard, J., Carton, D., et al. 2019, *MNRAS*, 489, 224, doi: [10.1093/mnras/stz2114](https://doi.org/10.1093/mnras/stz2114)
- Pessa, I., Schinnerer, E., Belfiore, F., et al. 2021, *A&A*, 650, A134, doi: [10.1051/0004-6361/202140733](https://doi.org/10.1051/0004-6361/202140733)
- Pillepich, A., Springel, V., Nelson, D., et al. 2018a, *MNRAS*, 473, 4077, doi: [10.1093/mnras/stx2656](https://doi.org/10.1093/mnras/stx2656)
- Pillepich, A., Nelson, D., Hernquist, L., et al. 2018b, *MNRAS*, 475, 648, doi: [10.1093/mnras/stx3112](https://doi.org/10.1093/mnras/stx3112)
- Pillepich, A., Nelson, D., Springel, V., et al. 2019, *MNRAS*, 490, 3196, doi: [10.1093/mnras/stz2338](https://doi.org/10.1093/mnras/stz2338)
- Popesso, P., Concas, A., Cresci, G., et al. 2023, *MNRAS*, 519, 1526, doi: [10.1093/mnras/stac3214](https://doi.org/10.1093/mnras/stac3214)
- Portinari, L., Chiosi, C., & Bressan, A. 1998, *A&A*, 334, 505, doi: [10.48550/arXiv.astro-ph/9711337](https://doi.org/10.48550/arXiv.astro-ph/9711337)
- Revalski, M., Rafelski, M., Henry, A., et al. 2024, *ApJ*, 966, 228, doi: [10.3847/1538-4357/ad382c](https://doi.org/10.3847/1538-4357/ad382c)
- Rosales-Ortega, F. F., Sánchez, S. F., Iglesias-Páramo, J., et al. 2012, *ApJL*, 756, L31, doi: [10.1088/2041-8205/756/2/L31](https://doi.org/10.1088/2041-8205/756/2/L31)
- Sánchez, S. F. 2020, *ARA&A*, 58, 99, doi: [10.1146/annurev-astro-012120-013326](https://doi.org/10.1146/annurev-astro-012120-013326)
- Sánchez, S. F., Kennicutt, R. C., Gil de Paz, A., et al. 2012, *A&A*, 538, A8, doi: [10.1051/0004-6361/201117353](https://doi.org/10.1051/0004-6361/201117353)
- Sánchez, S. F., Rosales-Ortega, F. F., Jungwiert, B., et al. 2013, *A&A*, 554, A58, doi: [10.1051/0004-6361/201220669](https://doi.org/10.1051/0004-6361/201220669)
- Sánchez, S. F., Avila-Reese, V., Hernandez-Toledo, H., et al. 2018, *RMxAA*, 54, 217, doi: [10.48550/arXiv.1709.05438](https://doi.org/10.48550/arXiv.1709.05438)
- Sánchez, S. F., Barrera-Ballesteros, J. K., López-Cobá, C., et al. 2019, *MNRAS*, 484, 3042, doi: [10.1093/mnras/stz019](https://doi.org/10.1093/mnras/stz019)
- Sánchez-García, M., Pereira-Santaella, M., García-Burillo, S., et al. 2022, *A&A*, 659, A102, doi: [10.1051/0004-6361/202141963](https://doi.org/10.1051/0004-6361/202141963)
- Sánchez-Menguiano, L., Sánchez Almeida, J., Muñoz-Tuñón, C., et al. 2019, *ApJ*, 882, 9, doi: [10.3847/1538-4357/ab3044](https://doi.org/10.3847/1538-4357/ab3044)
- Sanders, R. L., Shapley, A. E., Kriek, M., et al. 2018, *ApJ*, 858, 99, doi: [10.3847/1538-4357/aabcdb](https://doi.org/10.3847/1538-4357/aabcdb)
- Schaefer, A. L., Tremonti, C., Kauffmann, G., et al. 2022, *ApJ*, 930, 160, doi: [10.3847/1538-4357/ac651a](https://doi.org/10.3847/1538-4357/ac651a)
- Schaye, J., Crain, R. A., Bower, R. G., et al. 2015, *MNRAS*, 446, 521, doi: [10.1093/mnras/stu2058](https://doi.org/10.1093/mnras/stu2058)
- Schmidt, M. 1959, *ApJ*, 129, 243, doi: [10.1086/146614](https://doi.org/10.1086/146614)
- Somerville, R. S., & Davé, R. 2015, *ARA&A*, 53, 51, doi: [10.1146/annurev-astro-082812-140951](https://doi.org/10.1146/annurev-astro-082812-140951)
- Sparre, M., Hayward, C. C., Springel, V., et al. 2015, *MNRAS*, 447, 3548, doi: [10.1093/mnras/stu2713](https://doi.org/10.1093/mnras/stu2713)
- Speagle, J. S., Steinhardt, C. L., Capak, P. L., & Silverman, J. D. 2014, *ApJS*, 214, 15, doi: [10.1088/0067-0049/214/2/15](https://doi.org/10.1088/0067-0049/214/2/15)
- Springel, V., & Hernquist, L. 2003, *MNRAS*, 339, 289, doi: [10.1046/j.1365-8711.2003.06206.x](https://doi.org/10.1046/j.1365-8711.2003.06206.x)
- Springel, V., White, S. D. M., Tormen, G., & Kauffmann, G. 2001, *Monthly Notices of the Royal Astronomical Society*, 328, 726, doi: [10.1046/j.1365-8711.2001.04912.x](https://doi.org/10.1046/j.1365-8711.2001.04912.x)
- Springel, V., Pakmor, R., Pillepich, A., et al. 2018, *MNRAS*, 475, 676, doi: [10.1093/mnras/stx3304](https://doi.org/10.1093/mnras/stx3304)
- Thorp, M. D., Ellison, S. L., Pan, H.-A., et al. 2022, *MNRAS*, 516, 1462, doi: [10.1093/mnras/stac2288](https://doi.org/10.1093/mnras/stac2288)
- Thorp, M. D., Ellison, S. L., Simard, L., Sánchez, S. F., & Antonio, B. 2019, *MNRAS*, 482, L55, doi: [10.1093/mnrasl/sly185](https://doi.org/10.1093/mnrasl/sly185)
- Tomczak, A. R., Quadri, R. F., Tran, K.-V. H., et al. 2016, *ApJ*, 817, 118, doi: [10.3847/0004-637X/817/2/118](https://doi.org/10.3847/0004-637X/817/2/118)
- Torrey, P., Vogelsberger, M., Genel, S., et al. 2014, *MNRAS*, 438, 1985, doi: [10.1093/mnras/stt2295](https://doi.org/10.1093/mnras/stt2295)
- Torrey, P., Wellons, S., Ma, C.-P., Hopkins, P. F., & Vogelsberger, M. 2017, *MNRAS*, 467, 4872, doi: [10.1093/mnras/stx370](https://doi.org/10.1093/mnras/stx370)
- Torrey, P., Vogelsberger, M., Hernquist, L., et al. 2018, *MNRAS*, 477, L16, doi: [10.1093/mnrasl/sly031](https://doi.org/10.1093/mnrasl/sly031)
- Torrey, P., Vogelsberger, M., Marinacci, F., et al. 2019, *MNRAS*, 484, 5587, doi: [10.1093/mnras/stz243](https://doi.org/10.1093/mnras/stz243)
- Toyouchi, D., & Chiba, M. 2015, *ApJ*, 810, 18, doi: [10.1088/0004-637X/810/1/18](https://doi.org/10.1088/0004-637X/810/1/18)
- Trayford, J. W., & Schaye, J. 2019, *MNRAS*, 485, 5715, doi: [10.1093/mnras/stz757](https://doi.org/10.1093/mnras/stz757)

- Tremonti, C. A., Heckman, T. M., Kauffmann, G., et al. 2004, *ApJ*, 613, 898, doi: [10.1086/423264](https://doi.org/10.1086/423264)
- van de Sande, J., Fraser-McKelvie, A., Fisher, D. B., et al. 2024, in *IAU Symposium*, Vol. 377, *Early Disk-Galaxy Formation from JWST to the Milky Way*, ed. F. Tabatabaei, B. Barbuy, & Y.-S. Ting, 27–33, doi: [10.1017/S1743921323001138](https://doi.org/10.1017/S1743921323001138)
- Vogelsberger, M., Genel, S., Sijacki, D., et al. 2013, *MNRAS*, 436, 3031, doi: [10.1093/mnras/stt1789](https://doi.org/10.1093/mnras/stt1789)
- Vulcani, B., Poggianti, B. M., Tonnesen, S., et al. 2020, *ApJ*, 899, 98, doi: [10.3847/1538-4357/aba4ae](https://doi.org/10.3847/1538-4357/aba4ae)
- Wang, E., & Lilly, S. J. 2023, *ApJ*, 955, 55, doi: [10.3847/1538-4357/acecfd](https://doi.org/10.3847/1538-4357/acecfd)
- Wang, Y., Vogelsberger, M., Xu, D., et al. 2018, arXiv e-prints. <https://arxiv.org/abs/1811.06545>
- Weinberger, R., Springel, V., Hernquist, L., et al. 2017, *MNRAS*, 465, 3291, doi: [10.1093/mnras/stw2944](https://doi.org/10.1093/mnras/stw2944)
- Wuyts, S., Förster Schreiber, N. M., Nelson, E. J., et al. 2013, *ApJ*, 779, 135, doi: [10.1088/0004-637X/779/2/135](https://doi.org/10.1088/0004-637X/779/2/135)
- Zhu, G. B., Barrera-Ballesteros, J. K., Heckman, T. M., et al. 2017, *MNRAS*, 468, 4494, doi: [10.1093/mnras/stx740](https://doi.org/10.1093/mnras/stx740)